Biological applications and transmission electron microscopy investigation of mesoporous silica nanoparticles

by

Brian G. Trewyn

A dissertation submitted to the graduate faculty in partial

fulfillment of the requirements for the degree of

DOCTOR OF PHILOSOPHY

Major: Inorganic Chemistry

Program of Study Committee:
Victor S.-Y. Lin, Major Professor
Robert J. Angelici
L. Keith Woo
Amy H. Andreotti
L. Scott Chumbley

Iowa State University

Ames, Iowa

2006

Graduate College
Iowa State University

This is to certify that the doctoral dissertation of

Brian G. Trewyn

has met the thesis requirements of Iowa State University.

Major Professor

For the Major Program

Imagination is more important than knowledge.

If we knew what it was we were doing, it would not be called research, would it?

- Albert Einstein

TABLE OF CONTENTS

ABSTRACT

The research presented and discussed within involves the development of novel biological applications of mesoporous silica nanoparticles (MSN) and an investigation of mesoporous material by transmission electron microscopy (TEM). Mesoporous silica nanoparticles organically functionalized shown to undergo endocytosis in cancer cells and drug release from the pores was controlled intracellularly and intercellularly. Transmission electron microscopy investigations demonstrated the variety of morphologies produced in this field of mesoporous silica nanomaterial synthesis.

A series of room-temperature ionic liquid (RTIL) containing mesoporous silica nanoparticle (MSN) materials with various particle morphologies, including spheres, ellipsoids, rods, and tubes, were synthesized. By changing the RTIL template, the pore morphology was tuned from the MCM-41 type of hexagonal mesopores to rotational moiré type of helical channels, and to wormhole-like porous structures. These materials were used as controlled release delivery nanodevices to deliver antibacterial ionic liquids against *Escherichia coli K12*.

The involvement of a specific organosiloxane function group, covalently attached to the exterior of fluorescein doped mesoporous silica nanoparticles (FITC-MSN), on the degree and kinetics of endocytosis in cancer and plant cells was investigated. The kinetics of endocystosis of TEG coated FITC-MSN is significantly quicker than FITC-MSN as determined by flow cytometry experiments. The fluorescence confocal microscopy investigation showed the endocytosis of TEG coated-FITC MSN triethylene glycol grafted fluorescein doped MSN (TEG coated-FITC MSN) into both HeLa cells and Tobacco root protoplasts.

Once the synthesis of a controlled-release delivery system based on MCM-41-type mesoporous silica nanorods capped by disulfide bonds with superparamagnetic iron oxide nanparticles was completed. The material was characterized by general methods and the dosage and kinetics of the antioxidant dependent release was measured. Finally, the biological interaction of the material was determined along with TEM measurements. An electron microscopy investigation proved that the pore openings of the MSN were indeed blocked by the Fe_3O_4 nanoparticles. The biological interaction investigation demonstrated Fe_3O_4-capped MSN endocytosis into HeLa cells. Not only does the material enter the cells through endocytosis, but it seems that fluorescein was released from the pores, most probably caused by disulfide bond reducing molecules, antioxidants. In addition to endocytosis and release, the Fe_3O_4-capped MSN propelled the cells across a cuvette upon induction of a magnet force.

Finally, an important aspect of materials characterization is transmission electron microscopy. A TEM investigation demonstrated that incorporating different functional groups during the synthesis (co-condensation) changed the particle and pore morphologies.

CHAPTER 1. GENERAL INTRODUCTION

Dissertation Organization

This dissertation begins with general information important in understanding the research presented within. The following three chapters are complete scientific manuscripts, while the fifth chapter is a transmission electron microscopy investigation on various mesoporous materials that were produced in this laboratory. The sixth and final chapter contains general conclusions and points to directions of future projects.

Overview

Over the past two decades, the distinctions among material science, chemistry, and biology have become increasingly indistinguishable. Scientists in these fields have thus become ever more dependent upon one another's expertise. This fact is exemplified in research pertaining to mesoporous silica materials. In this chapter, an overview of mesoporous silica materials, including their discovery, synthesis and mechanism of formation, characterization, and applications in both the fields of catalysis and biology are presented and discussed.

Mesoporous Silica Materials

Discovery

Since the discovery of organic surfactant templating methods for preparing mesoporous silica materials such as MCM-41/48,[1,2] SBA-15,[3] MSU-n,[4] KIT-1,[5] and FSM-16,[6,7] the field of ordered materials has undergone extensive investigation regarding synthesis, characterization, and applications. Porous materials are broadly classified by IUPAC on the basis of pore diameter into three catagories: microporous (<2 nm), mesoporous (2-50 nm), and macroporous (>50 nm) materials. The best-known microporous materials are zeolites, which are natural or synthetic hydrated aluminosilicate with an open three-dimensional crystal structure.[8] Zeolites are used for separating mixtures by selective absorption, in sorption pumps for vacuum systems, and in ion exchange. Unfortunately, applications with zeolites are limited by the relatively small pore sizes available. Therefore, the research discussed herein focuses on mesoporous silica materials discovered in 1992 by researchers at the Mobil Research and Development Corporation.[1,2] The researchers designated this family of materials MCM-41 (Mobile Composite of Matter) following the original reaction of aluminosilcate gels in the presence of a quaternary ammonium surfactant template. The MCM-41 family of mesoporous sieves consists of hexagonal array of uniform mesopores, varying from 15 Å to greater than 100 Å in diameter. The surface area of these materials is generally greater than 700 m^2/g and have absorption capacities of 0.7 cm^3/g and greater. Concurrently with the Mobil Researchers, an independent group from Japan developed another method for synthesis of mesoporous material, designated FSM-16 (Folded Sheet Materials). Inagaki et al. successfully synthesized a highly ordered mesoporous material derived from layered polysilicate kanemite by an ion exchange reaction.[6,7] Though this material was synthesized by a different manner than the MCM-41 type, the pore size and surface area characteristics were similar, as were the powder X-ray diffraction patterns.

The research presented, reported, and discussed henceforth is based on the self-organized cationic surfactant-templated MCM-41.

Synthesis and Mechanism

In a typical synthesis, a silica source (tetraethyl orthosilicate or tetramethyl orthosilicate) was added in a dropwise fashion to a clear alkaline solution of a micelle-forming surfactant (generally long chain quaternary ammonium halides) at elevated temperature (~353 K) under vigorous stirring. After stirring at this increased temperature (~2 h) the as-synthesized MCM-41 was filtered and washed with aqueous and organic phase solvents. Two methods are currently employed to remove the structure-directing agents (surfactants). The first method for surfactant removal is calcination, which involves heating the as-synthesized MCM-41 to ≥773 K for several hours under a flow of N_2, O_2, or air. The other common method for surfactant removal is acid extraction. This method employs a solution of methanol (100 mL) and hydrochloric acid (37%, 1.0 mL), with 1.0 g as-synthesized MCM-41. This suspension is stirred vigorously at elevated temperature (333 K) for several hours (4-8 h). The latter method of surfactant removal will be addressed further below.

A mechanism, coined as liquid crystal templating, for the formation of MCM-41 type materials was proposed in Mobile’s Nature paper in 1992.[1] In the liquid crystal templating mechanism, the formation of surfactant micelles, induced by the addition of silicate anions, and followed by polymerization, results in the generation of the MCM-41 structure (Figure 1). Later studies have shown that the synthesis of MCM-41 may occur with a surfactant template concentration below the critical micelle concentration; so the inorganic species, silicate in the case of silica MCM-41, plays a key role in triggering the supramolecular self-assembly. This mechanism was proposed and further discussed by Stucky and coworkers (Figure 2).[9] Additional evidence to corroborate this proposal is that shorter chain surfactants, such as $(C_{12}H_{25}N(CH_3)_3Br$, which do not form rod-like micelles in water, templated mesoporous silica. In addition MCM-41 silicas are synthesized at temperatures above 70 °C where rod-like micelles are not stable. The mechanism is triggered by electrostatic interactions, which correspond to the displacement of the counteranions of the surfactant by polycharged and polydentate inorganic anions.

This interaction leads to organic-inorganic ion pairs, which form pseudo-liquid crystal phases. This is followed by the base-catalyzed cross linking of the inorganic species and the formation of a rigid replica of the underlying liquid crystalline phase.[10]

Characterization

Following synthesis, the material must be characterized to determine particle and pore morphology, structure and surface details. The five main characterizing techniques used on most mesoporous materials are low angle powder X-ray diffraction (XRD), nitrogen adsorption/desorption, scanning electron microscopy (SEM), transmission electron microscopy (TEM), and, recently, solid state nuclear magnetic resonance (NMR). Adsorption analysis gives information about the porosity and surface area of the materials, while SEM gives particle size and morphology. Diffraction techniques and TEM supply insight to the degree of structural order. Finally, solid state NMR measurements provide details regarding the surfaces of MCM-41 materials.

a.) Powder X-ray Diffraction

Despite long-range order, these materials are amorphous in nature, as demonstrated by solid state NMR and high angle X-ray diffraction patterns. For this reason, X-ray diffraction analysis is generally measured at the low angle (0.5 - 10°). A typical example of a low angle powder XRD of silica MCM-41 is shown in figure 3a. The powder X-ray diffraction is the most rapid method to determine the nature and degree of pore order in the material. Generally, three or four peaks of varying intensity are observed, which can be indexed in a hexagonal pattern characteristic of MCM-41 materials.[2] These peaks observed in the low-angle 2-theta region can be indexed as d_{100}, d_{110}, d_{200}, and d_{210}. The simple hexagonal lattice is shown in figure 3b. The lattice parameter may also be obtained from the XRD via the equation: $a = 2d_{100}/\sqrt{3}$, which is the sum of pore diameter and wall thickness. Thus, by measuring the lattice parameter and pore diameter (see below) the wall thickness can be easily determined.

b.) Nitrogen sorption analysis

Nitrogen adsorption/desorption is an important aspect of material characterizing for the determination of pore size (diameter), pore volume, and surface area. Two calculation methods reported in the mid twentieth century facilitated the measurements of surface area and pore diameter/volume. Stephen Brunauer, P.H. Emmett, and Edward Teller developed a method employed to calculate the surface area.[11] This calculation, known as Brunauer-Emmett-Teller (BET), determines the surface area by measuring the adsorption of nonpolar gases (N_2, Ar). The calculation is modeled on the physical adsorption of gas on the surface of the material as a function of pressure.[12] Surface area determinations involve creating the conditions required to adsorb an average monolayer of gas molecules onto a sample. As pressure increases, the amount of gas adsorbed quickly rises due to the capillary condensation in mesopores. This gas condensation occurring in the mesopores allows the fine porous structure of the sample to be evaluated. The pressure is increased until saturation is reached when all mesopores are filled with liquid. The pressure is reduced incrementally, evaporating the condensed gas from the system. Upon desorption, a hysteresis is commonly observed in mesoporous materials. Hysteresis is the phenomenon in which the value of a physical property lags behind changes in the effect causing it. The hysteresis between the adsorption and desorption branches of the isotherm reveals information regarding pore size, volume, area, and shape. Hysteresis loops most likely arise from a combination of thermodynamic and network effects. The thermodynamic hysteresis may be due to capillary condensation and capillary evaporation occurring at higher and lower pressures, respectively. The network effect may be caused by a decrease in pore diameter at the mouths of the pores, much like a wine bottle. A typical isotherm produced by nonfunctional silica MCM-41 material can be seen in figure four, notice the hysteresis.

The pore diameter and pore volume calculations were developed by Elliot P. Barrett, Leslie G. Joyner, and Paul P. Halenda.[13] This calculation, known as BJH, assumes a similar theory to the BET of the adsorption/desorption process. The BJH is calculated when saturation is reached and all mesopores are filled by the adsorptive gas. The BJH calculates a pore diameter distribution, outputs a histogram, and an average pore size is reported. It applies only to the mesopores and small macropore size range. This calculation assumes the approximate cylindrical pore geometry.[12]

c.) Scanning and transmission electron microscopy

The next characterization techniques employed on MCM-41 type materials are scanning and transmission electron microscopy (SEM and TEM, respectively). Since low angle powder XRD provides insufficient information to draw definite conclusions on the structure of the materials, these two electron microscopy techniques are employed. Scanning electron microscopy utilizes a lower voltage electron beam (<20 kV) and is useful for determining exterior particle morphology to about 50,000x magnification. The shape and size of the nanoparticles are readily observed by SEM (Figure 5a). Transmission electron microscopy utilizes a stronger electron beam (~300 kV), and allows for the visualization of pores. Transmission electron microscopy is not a substitute for XRD, since only a small sampling is obtained. The magnification achievable by TEM is in the order of 300,000x. Transmission electron microscopy gives evidence in support of the powder XRD regarding pore structure and order (Figure 5b). Chapter five provides further insight on TEM measurements of mesoporous materials.

d.) Solid state nuclear magnetic resonance

Solid State NMR, with new advances in ultrafast magic angle spinning (MAS), provides improved tools for the investigation of MCM-41 surfaces. With this technique, high-resolution ^{1}H spectra, ^{1}H—^{13}C heteronuclear, and ^{1}H—^{29}Si heteronuclear correlation spectra can be obtained quickly and with small sample quantities.[14,15] The ^{29}Si NMR data allows for the estimation of the relative concentration of Q^{2} and Q^{3} silicon sites associated with geminal $(\text{-O-})_2Si(OH)_2$ and single $(\text{-O-})_3SiOH$ silanol groups, respectively. When the MCM-41 material is covalently functionalized with organosilanes, functionalization of MCM-41 with organosilanes is detailed below, the MAS spectra can also estimate the relative concentration of T^{3} and T^{2} sites associated with $(\equiv SiO-)_3SiR$ and $(\equiv SiO-)_2Si(OR')R$, respectively.

The first two characterizing methods, XRD and nitrogen adsoption, are the most frequently employed methods to characterize periodic mesoporous silica materials because of cost and technical availability. Electron microscopy and solid state NMR, while giving important data, have limits due to the cost of the instruments and the knowledge necessary to carry out such measurements.

Functionalization of MCM-41

The materials used in the following projects are modified through covalent linkage between functional groups (organosilanes) and silica framework. There are two well-known methods for functionalizing the MCM-41 materials. These methods include grafting (post-synthesis) and co-condensation (direct incorporation).

The former method, grafting, involves introducing organic functional groups by direct reaction of organosilanes to the surface of the mesoporous material. One advantage of the grafting method of surface functionalization is that the as-synthesized material can be calcined before functionalizing to ensure the surfactant is completely removed. Functionalizing MCM-41 material through the grafting method has several disadvantages. The distribution and concentration of functional groups are influenced by the reactivity of the organosilane and the accessibility of surface silanols, which are limited by diffusion and steric factors. Essentially, grafting organosilanes allows, almost exclusively, for coverage on the exterior and at the ends of the pores.

The latter method, co-condensation, involves hydrolytically condensing organosilanes with conventional silica sources such as tetraethyl orthosilicate.[16,17] The co-condensation method has advantages over the grafting method in that it offers a short, one-pot preparation, which yields a mesoporous silica material with a homogeneous distribution of functional groups, in high loading. In 2002, Ozin and coworkers reported very high functional group loading, up to 62%, in mesoporous silica material through the co-condensation method.[18] The incorporation of the organosilanes in the synthesis does lead to interesting, unique particle morphologies.[19,20] The various organosilanes interact with the template-directing surfactants in a different manner than the silanols or silicates of MCM-41, giving rise to these different morphologies.

Applications of MCM-41

The unique characteristics of the MCM-41 family of materials -- including high surface area, well-defined pore shape, narrow pore size distribution, large pore volume, and high stability -- are conducive to a wide variety of noteworthy applications. These applications include, but are not limited to, heterogeneous catalysis and catalyst support,[21-38] heterogenization of homogeneous catalysts,[39-44] separation and adsorption processes,[32,45-50] drug delivery and controlled release,[51-62] and sensors.[56,63-75]

Heterogeneous catalysis systems display advantages over similar homogeneous systems, such as the ease of recovery and recycling of the active species. Heterogeneous catalysts are obviously attractive from environmental and economical points of view. The high surface area, large pore volume, and structure diversity allows for the selective adsorption of a variety of gases, liquids, and solids. One application of heterogeneous catalysis has been the development of a heterogeneous solid acid catalyst. This is advantageous over traditional homogeneous acid catalysts, since traditional homogenous acid catalysts necessitate the handling of hazardous chemicals. In 2002, Klier and coworkers reported the synthesis of propylsulfonic acid-functionalized SBA-15.[76] This material catalyzed coupling reactions of alcohols to ethers with high selectivity.

Organic functionality is not the only type of chemical functionality to be incorportated into mesoporous materials. The incorporation of organic ligand groups are often used for the entrapment of metal components in MCM-41. Recently, Thiel and coworkers covalently functionalized MCM-41 with 3-(2-pyridyl)-1-pyrazoylacetamide ligands via a co-condensation method.[77] By adding a solution of oxodiperoxomolybdenum, a heterogeneous MoO(O_2) complex formed with all chemically accessible ligands. This catalyst worked as a highly active catalyst for the epoxidation of cyclooctene with t-butyl hydroperoxides, with minimal leaching.

Another important function of MCM-41 type material involves their interaction with biomolecules and biological systems. Various publications document the use of MCM-41 as solid supports for enzymes -- by covalent attachment, electrostatic interactions, and hydrogen bonding. Immobilized enzymes are being increasingly used as catalysts in many commercial applications, owing to their ease of separation and enhanced thermal and pH stability. In 2003, Choudary and coworkers reported the preparation of immobilized α-chymotrypsin on MCM-41, with a significant protein loading of 170 mg g^{-1}. In this case, the enzyme was stirred with MCM-41 in aqueous tris-HCl buffer (pH 7.2), where the α-chymotrypsin is immobilized via a simple electrostatic interaction.[78] More recently, in 2004, Duan and coworkers immobilized lipase in the pores of MCM-41 through hydrogen bonding interactions between the weakly acidic hydroxyl groups of the support and the enzyme. By treating the immobilized enzyme with vinyltrimethoxysilane, the activity of triacetylglycerol hydrolysis remained constant over five cycles.[79]

Recently, researchers have demonstrated endocytosis of MCM-41 material into various cellular systems. In 2005, Mou *et al.* synthesized functionalized nanosized mesoporous silicas to be used as fluorescence cell tags in both fibroblast and human masenchymal stem cells.[32,80] Earlier, Radu *et al.* showed the endocytosis of MCM-41 that was covalently capped with PAMAM dendrimer and complexed with plasmid DNA.[81] Also, in 2005 Lin *et al.* demonstrated the synthesis of a controlled-release delivery system that is based on MCM-41 capped with superparamagnetic iron oxide nanoparticles and was stimuli-responsive and chemically inert to guest molecules entrapped in the pores.[82]

This review shows that a vast field of new and exciting periodic mesoporous materials are rapidly emerging from research institutes around the world. Diverse applications of periodic mesoporous materials continue to stimulate interest in many fields including chemistry, material science, and biology. The mesoporous silica nanoparticle (MSN) materials developed in our labs possess a variety of properties to make them potentially useful at the cellular level. Our goal was to investigate the potential applications of MSNs as antibacterial agents, vehicles for animal and plant cell endocytosis, and stimuli-responsive controlled release material. In addition, a final goal was the investigation of various mesoporous materials using transmission electron microscopy.

References

(1) Kresge, C. T.; Leonowicz, M. E.; Roth, W. J.; Vartuli, J. C.; Beck, J. S. *Nature (London, United Kingdom)* 1992, *359*, 710-12.

(2) Beck, J. S.; Vartuli, J. C.; Roth, W. J.; Leonowicz, M. E.; Kresge, C. T.; Schmitt, K. D.; Chu, C. T. W.; Olson, D. H.; Sheppard, E. W.; et al. *Journal of the American Chemical Society* 1992, *114*, 10834-43.

(3) Zhao, D.; Feng, J.; Huo, Q.; Melosh, N.; Frederickson, G. H.; Chmelka, B. F.; Stucky, G. D. *Science (Washington, D. C.)* 1998, *279*, 548-552.

(4) Bagshaw, S. A.; Prouzet, E.; Pinnavaia, T. J. *Science (Washington, D. C.)* 1995, *269*, 1242-4.

(5) Ryoo, R.; Kim, J. M.; Ko, C. H.; Shin, C. H. *Journal of Physical Chemistry* 1996, *100*, 17718-17721.

(6) Inagaki, S.; Fukushima, Y.; Kuroda, K. *Journal of the Chemical Society, Chemical Communications* 1993, 680-2.

(7) Inagaki, S.; Koiwai, A.; Suzuki, N.; Fukushima, Y.; Kuroda, K. *Bulletin of the Chemical Society of Japan* 1996, *69*, 1449-1457.

(8) Daintith, J. *A Dictionary of Chemistry*; 3 ed.; Oxford University Press: New York, 1996.

(9) Firouzi, A.; Kumar, D.; Bull, L. M.; Besier, T.; Sieger, P.; Huo, Q.; Walker, S. A.; Zasadzinski, J. A.; Glinka, C.; Nicol, J.; Margolese, D.; Stucky, G. D.; Chmelka, B. F. *Science (Washington, D. C.)* 1995, *267*, 1138-1143.

(10) Yang, P.; Editor *The Chemistry of Nanostructured Materials*, 2003.

(11) Brunauer, S.; Emmett, P. H.; Teller, E. *Journal of the American Chemical Society* 1938, *60*, 309-19.

(12) Kruk, M.; Jaroniec, M. *Chemistry of Materials* 2001, *13*, 3169-3183.

(13) Joyner, L. G.; Barrett, E. P.; Skold, R. *Journal of the American Chemical Society* 1951, *73*, 3155-8.

(14) Trebosc, J.; Wiench, J. W.; Huh, S.; Lin, V. S. Y.; Pruski, M. *Journal of the American Chemical Society* 2005, *127*, 7587-7593.

(15) Trebosc, J.; Wiench, J. W.; Huh, S.; Lin, V. S. Y.; Pruski, M. *Journal of the American Chemical Society* 2005, *127*, 3057-3068.

(16) Burkett, S. L.; Sims, S. D.; Mann, S. *Chemical Communications (Cambridge)* 1996, 1367-1368.

(17) Macquarrie, D. J. *Chemical Communications (Cambridge)* 1996, 1961-1962.

(18) Kruk, M.; Asefa, T.; Jaroniec, M.; Ozin Geoffrey, A. *Journal of the American Chemical Society* 2002, *124*, 6383-92.

(19) Huh, S.; Wiench, J. W.; Trewyn, B. G.; Song, S.; Pruski, M.; Lin, V. S. Y. *Chemical Communications (Cambridge, United Kingdom)* 2003, 2364-2365.

(20) Huh, S.; Wiench, J. W.; Yoo, J.-C.; Pruski, M.; Lin, V. S. Y. *Chemistry of Materials* 2003, *15*, 4247-4256.

(21) Aprile, C.; Abad, A.; Garcia, H.; Corma, A. *Journal of Materials Chemistry* 2005, *15*, 4408-4413.

(22) Brunel, D.; Blanc, A. C.; Galarneau, A.; Fajula, F. *Catalysis Today* 2002, *73*, 139-152.

(23) Chai, G. S.; Shin, I. S.; Yu, J.-S. *Advanced Materials (Weinheim, Germany)* 2004, *16*, 2057-2061.

(24) Cho, Y. S.; Park, J. C.; Lee, B.; Kim, Y.; Yi, J. *Catalysis Letters* 2002, *81*, 89-96.

(25) Corma, A. *Chemical Reviews (Washington, D. C.)* 1997, *97*, 2373-2419.

(26) Dubey, A.; Choi, M.; Ryoo, R. *Green Chemistry* 2006, *8*, 144-146.

(27) Huh, S.; Chen, H.-T.; Wiench, J. W.; Pruski, M.; Lin, V. S. Y. *Angewandte Chemie, International Edition* 2005, *44*, 1826-1830.

(28) Li, Z.; Gao, L.; Zheng, S. *Applied Catalysis, A: General* 2002, *236*, 163-171.

(29) Lin, V. S. Y.; Radu, D. R.; Han, M.-K.; Deng, W.; Kuroki, S.; Shanks, B. H.; Pruski, M. *Journal of the American Chemical Society* 2002, *124*, 9040-9041.

(30) Patra, C. R.; Ghosh, A.; Mukherjee, P.; Sastry, M.; Kumar, R. *Studies in Surface Science and Catalysis* 2002, *141*, 641-646.

(31) Rac, B.; Molnar, A.; Forgo, P.; Mohai, M.; Bertoti, I. *Journal of Molecular Catalysis A: Chemical* 2006, *244*, 46-57.

(32) Radu, D. R.; Lai, C.-Y.; Huang, J.; Shu, X.; Lin, V. S. Y. *Chemical Communications (Cambridge, United Kingdom)* 2005, 1264-1266.

(33) Thomas, J. M. *Journal of Molecular Catalysis A: Chemical* 1999, *146*, 77-85.

(34) Wang, X.; Tseng, Y.-H.; Chan, J. C. C.; Cheng, S. *Microporous and Mesoporous Materials* 2005, *85*, 241-251.

(35) Xiang, S.; Zhang, Y.; Xin, Q.; Li, C. *Angewandte Chemie, International Edition* 2002, *41*, 821-824.

(36) Xiao, F.-S. *Topics in Catalysis* 2005, *35*, 9-24.

(37) Zhang, J.-L.; Liu, Y.-L.; Che, C.-M. *Chemical Communications (Cambridge, United Kingdom)* 2002, 2906-2907.

(38) Zheng, Y.; Su, X.; Zhang, X.; Wei, W.; Sun, Y. *Studies in Surface Science and Catalysis* 2005, *156*, 205-212.

(39) Kureshy, R. I.; Ahmad, I.; Khan, N.-u. H.; Abdi, S. H. R.; Pathak, K.; Jasra, R. V. *Tetrahedron: Asymmetry* 2005, *16*, 3562-3569.

(40) Fuerte, A.; Corma, A.; Sanchez, F. *Catalysis Today* 2005, *107-108*, 404-409.

(41) Gonzalez-Arellano, C.; Corma, A.; Iglesias, M.; Sanchez, F. *Advanced Synthesis & Catalysis* 2004, *346*, 1316-1328.

(42) Peng, Q.; Yang, Y.; Yuan, Y. *Journal of Molecular Catalysis A: Chemical* 2004, *219*, 175-181.

(43) Kucherov, A. V.; Kramareva, N. V.; Finashina, E. D.; Koklin, A. E.; Kustov, L. M. *Journal of Molecular Catalysis A: Chemical* 2003, *198*, 377-389.

(44) Alcon, M. J.; Corma, A.; Iglesias, M.; Sanchez, F. *Journal of Organometallic Chemistry* 2002, *655*, 134-145.

(45) Ernst, S.; Hartmann, M.; Munsch, S.; Thiel, H. *Studies in Surface Science and Catalysis* 2004, *154B,* 2020-2026.

(46) Mehraban, Z.; Farzaneh, F. *Microporous and Mesoporous Materials* 2006, *88*, 84-90.

(47) Shiraishi, Y.; Nishimura, G.; Hirai, T.; Komasawa, I. *Industrial & Engineering Chemistry Research* 2002, *41*, 5065-5070.

(48) Song, C.; Xu, X.; Andresen, J. M.; Miller, B. G.; Scaroni, A. W. *Studies in Surface Science and Catalysis* 2004, *153*, 411-416.

(49) Xu, X.; Song, C.; Andresen, J. M.; Miller, B. G.; Scaroni, A. W. *International Journal of Environmental Technology and Management* 2004, *4*, 32-52.

(50) Zhao, Y. X.; Ding, M. Y.; Chen, D. P. *Analytica Chimica Acta* 2005, *542*, 193-198.

(51) Andersson, J.; Rosenholm, J.; Areva, S.; Linden, M. *Chemistry of Materials* 2004, *16*, 4160-4167.

(52) Casasus, R.; Marcos, M. D.; Martinez-Manez, R.; Ros-Lis, J. V.; Soto, J.; Villaescusa, L. A.; Amoros, P.; Beltran, D.; Guillem, C.; Latorre, J. *Journal of the American Chemical Society* 2004, *126*, 8612-8613.

(53) Fornasieri, G.; Badaire, S.; Backov, R.; Mondain-Monval, O.; Zakri, C.; Poulin, P. *Advanced Materials (Weinheim, Germany)* 2004, *16*, 1094-1097.

(54) Gruenhagen, J. A.; Lai, C.-Y.; Radu, D. R.; Lin, V. S. Y.; Yeung, E. S. *Applied Spectroscopy* 2005, *59*, 424-431.

(55) Mal, N. K.; Fujiwara, M.; Tanaka, Y. *Nature (London, United Kingdom)* 2003, *421*, 350-353.

(56) Ostafin, A. E.; Burgess, J. P.; Mizukami, H. *Tissue Engineering and Novel Delivery Systems* 2004, 483-503.

(57) Sayari, A. *Chemistry of Nanostructured Materials* 2003, 39-68.

(58) Tourne-Peteilh, C.; Lerner, D. A.; Chamay, C.; Nicole, L.; Begu, S.; Devoisselle, J.-M. *ChemPhysChem* 2003, *4*, 281-286.

(59) Tozuka, Y.; Oguchi, T.; Yamamoto, K. *Pharmaceutical Research* 2003, *20*, 926-930.

(60) Trewyn, B. G.; Whitman, C. M.; Lin, V. S. Y. *Nano Letters* 2004, *4*, 2139-2143.

(61) Vallet-Regi, M.; Doadrio, J. C.; Doadrio, A. L.; Izquierdo-Barba, I.; Perez-Pariente, J. *Solid State Ionics* 2004, *172*, 435-439.

(62) Zhu, Y.; Shi, J.; Shen, W.; Chen, H.; Dong, X.; Ruan, M. *Nanotechnology* 2005, *16*, 2633-2638.

(63) Balaji, T.; Sasidharan, M.; Matsunaga, H. *Analytical and Bioanalytical Chemistry* 2006, *384*, 488-494.

(64) Cabot, A.; Arbiol, J.; Cornet, A.; Morante, J. R.; Chen, F.; Liu, M. *Thin Solid Films* 2003, *436*, 64-69.

(65) Descalzo, A. B.; Marcos, M. D.; Martinez-Manez, R.; Soto, J.; Beltran, D.; Amoros, P. *Journal of Materials Chemistry* 2005, *15*, 2721-2731.

(66) Feng, Y.; Yao, R.; Zhang, L. *Materials Chemistry and Physics* 2004, *89*, 312-315.

(67) Konorov, S. O.; Mitrokhin, V. P.; Smirnova, I. V.; Fedotov, A. B.; Sidorov-Biryukov, D. A.; Zheltikov, A. M. *Chemical Physics Letters* 2004, *394*, 1-4.

(68) Metivier, R.; Leray, I.; Lebeau, B.; Valeur, B. *Journal of Materials Chemistry* 2005, *15*, 2965-2973.

(69) Onida, B.; Borello, L.; Fiorilli, S.; Bonelli, B.; Arean, C. O.; Garrone, E. *Chemical Communications (Cambridge, United Kingdom)* 2004, 2496-2497.

(70) Radu, D. R.; Lai, C.-Y.; Wiench, J. W.; Pruski, M.; Lin, V. S. Y. *Journal of the American Chemical Society* 2004, *126*, 1640-1641.

(71) Sasahara, T.; Kido, A.; Ishihara, H.; Sunayama, T.; Egashira, M. *Sensors and Actuators, B: Chemical* 2005, *B108*, 478-483.

(72) Wirnsberger, G.; Scott, B. J.; Stucky, G. D. *Chemical Communications (Cambridge)* 2001, 119-120.

(73) Yantasee, W.; Fryxell, G. E.; Conner, M. M.; Lin, Y. *Journal of Nanoscience and Nanotechnology* 2005, *5*, 1537-1540.

(74) Yantasee, W.; Lin, Y.; Fryxell, G. E.; Wang, Z. *Electroanalysis* 2004, *16*, 870-873.

(75) Zhang, H.; Sun, Y.; Ye, K.; Zhang, P.; Wang, Y. *Journal of Materials Chemistry* 2005, *15*, 3181-3186.

(76) Shen, J. G. C.; Herman, R. G.; Klier, K. *Journal of Physical Chemistry B* 2002, *106*, 9975-9978.

(77) Jia, M.; Seifert, A.; Berger, M.; Giegengack, H.; Schulze, S.; Thiel, W. R. *Chemistry of Materials* 2004, *16*, 877-882.

(78) Fadnavis, N. W.; Bhaskar, V.; Kantam, M. L.; Choudary, B. M. *Biotechnology Progress* 2003, *19*, 346-351.

(79) Ma, H.; He, J.; Evans, D. G.; Duan, X. *Journal of Molecular Catalysis B: Enzymatic* 2004, *30*, 209-217.

(80) Lin, Y.-S.; Tsai, C.-P.; Huang, H.-Y.; Kuo, C.-T.; Hung, Y.; Huang, D.-M.; Chen, Y.-C.; Mou, C.-Y. *Chemistry of Materials* 2005, *17*, 4570-4573.

(81) Radu, D. R.; Lai, C.-Y.; Jeftinija, K.; Rowe, E. W.; Jeftinija, S.; Lin, V. S. Y. *Journal of the American Chemical Society* 2004, *126*, 13216-13217.

(82) Giri, S.; Trewyn, B. G.; Stellmaker, M. P.; Lin, V. S. Y. *Angewandte Chemie, International Edition* 2005, *44*, 5038-5044.

FIGURE LEGENDS

Figure 1. Liquid Crystal templating mechanism for the formation of MCM-41 [2].

Figure 2. Cooperative inorganic-surfactant templating mechanism [8].

Figure 3. (a) Typical low angle powder X-ray diffraction for MCM-41. (b) Simple hexagonal lattice index.

Figure 4. Typical nitrogen adsorption/desorption isotherm and pore diameter distribution (inset) calculated by BJH.

Figure 5. Typical SEM (a) and TEM (b) micrographs of nonfunctional MCM-41 silica.

Figure 1.

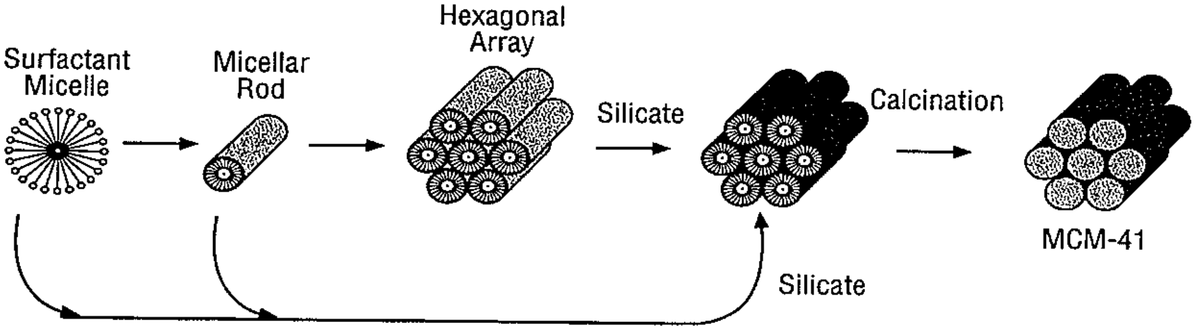
Surfactant Micelle
Micellar Rod
Hexagonal Array
Silicate
Calcination
MCM-41
Silicate

Figure 2.

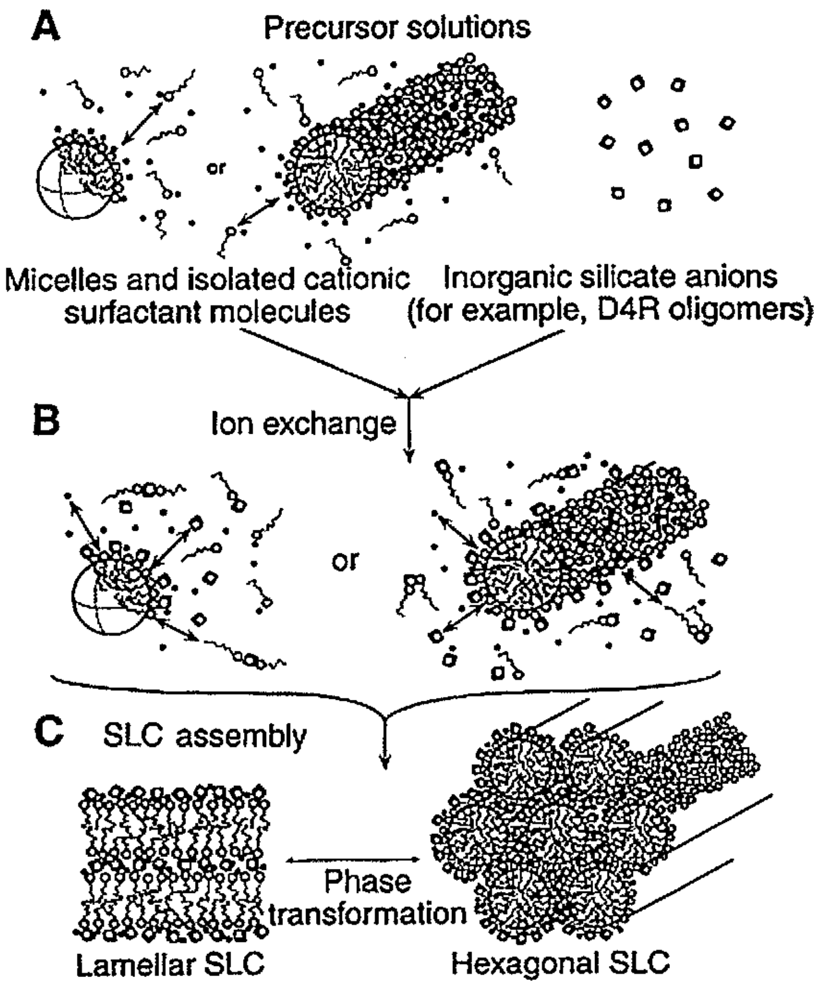
A
Precursor solutions
or
Micelles and isolated cationic surfactant molecules
Inorganic silicate anions (for example, D4R oligomers)
B
Ion exchange
or
C
SLC assembly
Phase transformation
Lamellar SLC
Hexagonal SLC

Figure 3a.

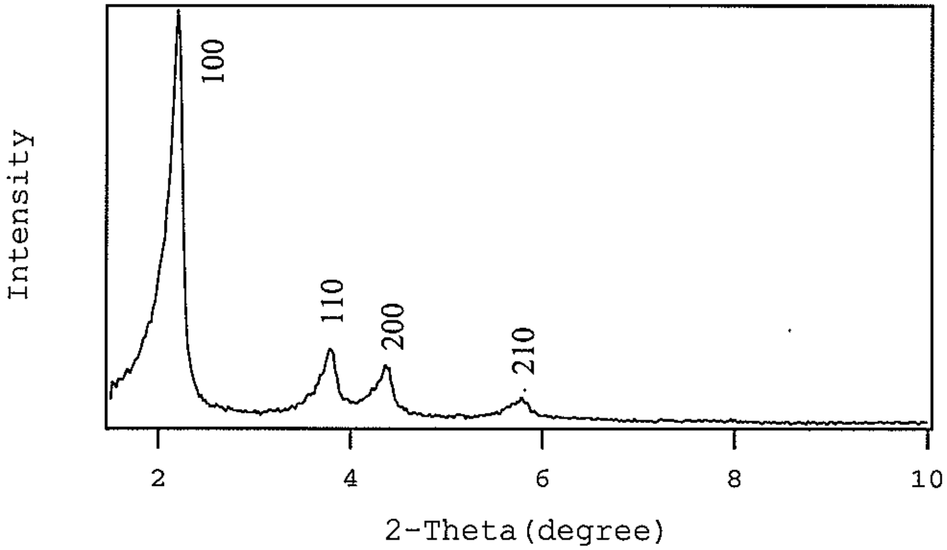

Figure 3b.

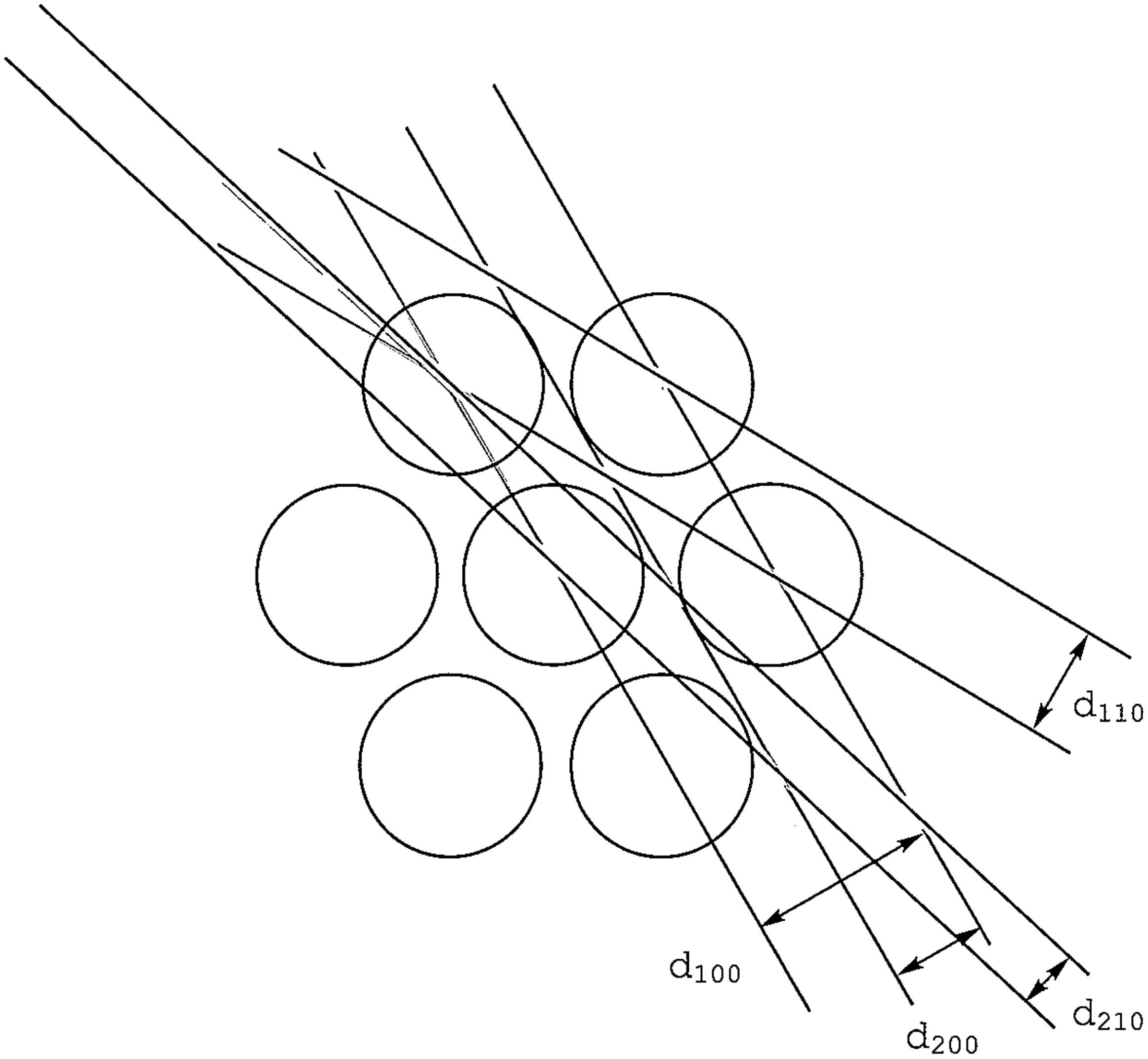

Figure 4.

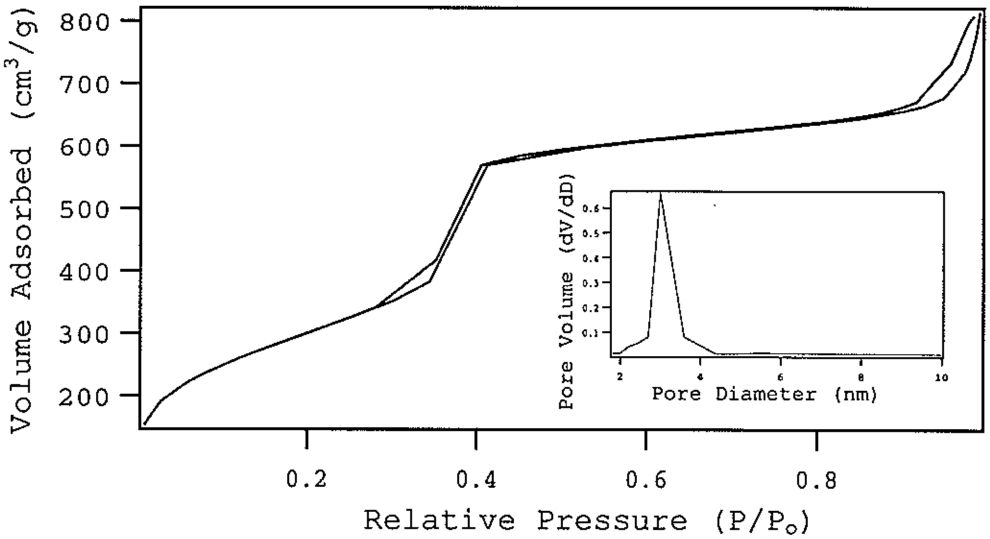
Volume Adsorbed (cm^3/g)
800
700
600
500
400
300
200
0.2
0.4
0.6
0.8
Relative Pressure (P/P$_o$)
Pore Volume (dV/dD)
0.6
0.5
0.4
0.3
0.2
0.1
2
4
6
8
10
Pore Diameter (nm)

Figure 5.

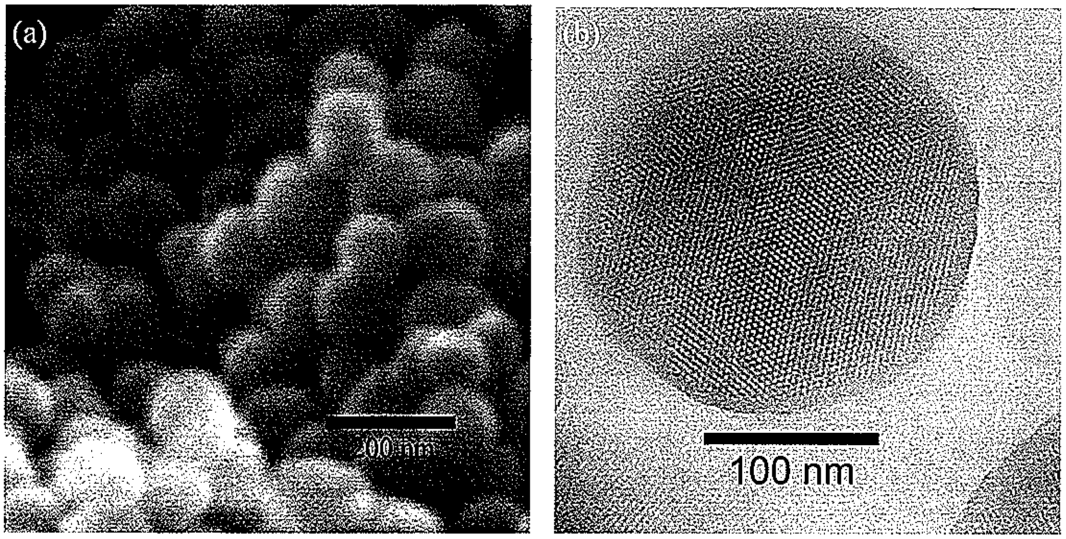

CHAPTER 2. MORPHOLOGICAL CONTROL OF ROOM-TEMPERATURE IONIC LIQUID TEMPLATED MESOPOROUS SILICA NANOPARTICLES FOR CONTROLLED RELEASE OF ANTIBACTERIAL AGENTS

A paper published in *NanoLetters* **2004**, *11*, 2139-2143.

Brian G. Trewyn, Chad M. Whitman, Victor S.-Y. Lin*

*Primary researcher and author

ABSTRACT. A series of room-temperature ionic liquid (RTIL) containing mesoporous silica nanoparticle (MSN) materials with various particle morphologies, including spheres, ellipsoids, rods, and tubes, were synthesized. By changing the RTIL template, the pore morphology was tuned from the MCM-41 type of hexagonal mesopores to rotational moiré type of helical channels, and to wormhole-like porous structures. These materials were used as controlled release delivery nanodevices to release antibacterial ionic liquids against *Escherichia coli K12*.

Structurally well-defined mesoporous silica materials, such as MCM-41/48,[1] SBA-15,[2] MSU-n,[3] KIT-1,[4] and FSM-16,[5] have recently attracted much attention for their potential applications in sensing,[6] catalysis,[7] and drug delivery.[8] These materials are typically synthesized by utilizing organic surfactants or block copolymers as structure-directing templates in acid- or base-catalyzed condensation of alkoxysilanes. Obviously, the realization of the aforementioned applications for mesoporous silica materials greatly depends on the ability of controlling not only the intra-particle, but also the inter-particle mass-transport processes. Therefore, it is important to develop methods to regulate both the pore and particle morphology of these materials.[9]

To this goal, several recent reports[10] have focused on the utilization of other amphiphilic molecules, such as room-temperature ionic liquids (RTILs), as templates for the synthesis of mesoporous silica materials. For example, Zhou *et. al.*[10a-c] have demonstrated that monolithic mesoporous silicas with either wormlike pores or lamellar super-microporous structures could be prepared by using 1-alkyl-3-methylimidazolium (C_nMIM, n = the number of carbons in the alkyl chain) chloride or tetrafluoroborate, respectively, as templates. Also, Dai and co-workers[10d] have successfully synthesized periodic mesoporous organosilica (PMO) materials by using two different C_nMIM bromide templates in the condensation reaction of bis(triethoxysilyl)ethane. Despite these recent advancements, no study has been reported on how the particle morphology (size and shape) could be regulated by these RTILs. Herein, we report on the synthesis and characterization of a series of mesoporous silica nanoparticle (MSN) materials with various porous structures and particle shapes, such as spheres, ellipsoids, rods, and tubes, by using different RTIL templates, such as 1-tetradecyl-3-methylimidazolium bromide ($C_{14}MIMBr$), 1-hexadecyl-3-methylimidazolium bromide ($C_{16}MIMBr$), 1-octadecyl-3-methylimidazolium bromide ($C_{18}MIMBr$), and 1-tetradecyloxymethyl-3-methylimidazolium chloride ($C_{14}OCMIMCl$), respectively (Figure 1). To study the mass-transport properties of the C_nMIM-MSN materials, we investigated the controlled release profiles of these materials by utilizing the RTIL templates as antibacterial agents against the Gram (-) microbe *Escherichia coli K12* as depicted in Figure 2. Our results indicated that the rates of RTIL release from the MSN materials are governed by the particle and pore morphology leading to different antibacterial activities.

First, we synthesized the C_{14}MIMBr, C_{16}MIMBr, and C_{18}MIMBr RTILs by reacting 1-methylimidazole (50 mmol) with 50 mmol of 1-bromotetradecane, 1-bromohexadecane, and 1-bromooctadecane, respectively, at 90 °C for 48 h. The products were purified by recrystallization in THF. The resulting white crystals were collected by filtration, and dried under vacuum at room temperature. The C_{14}OCMIMCl was prepared via a literature procedure.[11] In a typical procedure for the synthesis of the C_nMIM-MSN materials, a selected C_nMIM RTIL (2.74 mmol) was first dissolved in 480 mL of 15 mM NaOH(aq). The solution was heated to 80 °C, followed by a dropwise addition of tetraethyl orthosilicate (22.4 mmol) and stirred for 2 h to yield the desired C_nMIM-MSN material.

To characterize the mesoporous structures of the C_nMIM-MSN materials, the C_nMIM RTILs were extracted from the mesopores by refluxing the as-synthesized C_nMIM-MSN (500 mg) in 200 mL of methanolic solution of HCl (520 mM) for 48 h. As revealed by the transmission electron micrographs (TEM) in Figure 3, C_nMIM-MSNs synthesized with the four different RTIL templates exhibited different particle morphologies. For example, the $C_{14}MIM$-MSN material showed spherical particles with diameters ranging from 100 to 300 nm, as depicted in Figure 3a. Interestingly, upon replacing the $C_{14}MIMBr$ with other structurally similar RTILs with longer alkyl chains, such as $C_{16}MIMBr$, and $C_{18}MIMBr$ (Figure 3b, c), the shapes of the MSN materials transformed into ellipsoids and rods, respectively. Furthermore, substituting the $C_{16}MIM$ template with a similar sized $C_{14}OCMIM$ RTIL gave rise to the $C_{14}OCMIM$-MSN material (Figure 3d) consisted of tubular shaped particles.

The pore morphologies of the C_nMIM-templated MSNs were determined by nitrogen adsorption-desorption surface analysis (BET isotherms and BJH pore size distributions), TEM (Figure 3), and powder X-ray diffraction (XRD) spectroscopy (Figure 4). All four C_nMIM-MSN materials exhibited type IV BET isotherms. Also, the BJH average pore diameters of these materials increased as the organic regions of the RTILs lengthened (Table 1). Hexagonally packed mesoporous channels were clearly observed in the TEM micrographs of the C_{14}MIM- and C_{16}MIM-MSNs (Figure 3a, b). In addition, both materials exhibited diffraction patterns characteristic of hexagonal MCM-41 silicas, including (100), (110), (200), and (210) peaks as depicted in Figure 4a, b.

Interestingly, a pseudo-moiré rotational pattern of mesopores was observed in the TEM micrograph of the C_{18}MIM-MSN material (Figure 3c), where parallel mesopores are twisted in a helical nature along the long axis of the nanorods. This pore morphology is structurally similar to a chiral mesoporous silica material recently reported by Tatsumi and co-workers.[12] In contrast to Tatsumi's material, which was synthesized in the presence of a *chiral* surfactant template, the C_{18}MIM-MSN material was prepared by using an *achiral* surfactant (C_{18}MIMBr) as the structure-directing agent. As indicated by the arrow-pointed areas in Figure 3c, each visible fringe represents the (100) interplanar spacing. The distance between two fringes is one-sixth of a pitch or a 60° rotation through the center of the long axis. It is noteworthy that all the particles shown in Figure 3c appeared to have rotations of approximately 120° regardless of particle size. The powder

XRD analysis (Figure 4c) of the C_{18}MIM-MSN material further confirmed the twisted hexagonal ordering of the mesopores as evidenced by the diffraction pattern of an intense (100) peak along with a well-resolved (110) and a broadened (200) peaks. The handedness of the rotation (right- or left-handed) could not be determined from the TEM analysis. As discussed in Tatsumi's report,[12] the ratio of the left- and right-handedness of their chiral mesoporous silica material (65/35, left/right) was not entirely governed by the intrinsic chirality of the surfactant template since only the *L*-enantiomer of the chiral surfactant was employed. In our case, we hypothesized that, as the alkyl chain lengths of the C_nMIMBr increases from C_{14} to C_{18}, tighter intermolecular packing between the methylimidazolium head groups of the *achiral* C_{18}MIMBr molecules might have occurred. Given the planar structure of the imidazolium group, such tight packing would perhaps cause a staggered wadding of the C_{18}MIMBr molecules and twisted the micelles into a *helical* structure.

This assumption was further investigated by the TEM and XRD analyses of the C_{14}OCMIM-MSN material that was synthesized with C_{14}OCMIMCl, which is a similarly sized molecule in comparison with the C_{16}MIMBr that gave rise to a MCM-41 type mesoporous structure. The mesoporous structure of the C_{14}OCMIM-MSN material appeared to be disordered as indicated by a broad XRD diffraction peak at 4.22° representing superimposed (110) and (200) peaks (Figure 4d). The TEM micrograph shown in Figure 3d is also consistent with this observation. Given that the hydrophilic polar region of C_{14}OCMIM, with the ether moiety close to the methylimidazolium head group, is significantly larger of that of C_{16}MIM, the results support our theory that the micellar structure and packing is strongly influenced by the alkyl chain length of the alkylimidazolium template.

It is widely known that cationic surfactants possess antibacterial properties, several can be found in household soaps and detergents.[13] A recent report[11] in the literature has demonstrated the antibacterial activity of C_{14}OCMIMCl on both Gram (+) and Gram (-) microbes. The mechanism of the antibacterial activity of C_{14}OCMIMCl was attributed to the electrostatic interaction of phosphate groups on the microbial cell wall and the cationic methylimidazolium head group of the RTIL. Also, the organic tail region embeds itself in the lipid bilayer. This in turn leads to the free flow of electrolytes out of the microbe and causes the cell death. This is believed to be the mechanism of cell death for the other RTIL as well.

The antibacterial activities of the C_{16}MIMBr and C_{14}OCMIMCl were measured by three methods: disk diffusion assay, minimal inhibitory concentration (MIC), and minimal bactericidal concentration (MBC). The disk diffusion assay was determined by placing a 25 mm cellulose disk saturated with 15 mM of C_{16}MIMBr and C_{14}OCMIMCl in 100 mM phosphate buffer (pH 7.4) onto agar plates seeded with *E. coli K12.* As depicted in Figure 5, the results of the disk diffusion assay showed an average of 35 mm of microbial clearing for C_{16}MIMBr and C_{14}OCMIMCl. The control (a cellulose disk saturated with 100 mM phosphate buffer pH 7.4) showed no antibacterial activity (Figure 5c). The MIC and MBC concentrations were determined by dissolving ten different concentrations (10 to 100 mM) of C_{16}MIMBr and C_{14}OCMIMCl in broth media, inoculated in a 1:1 ratio with stock *E. coli K12* culture, and visually determining the lowest concentration that lacked bacteria growth for the MIC. The MBC was measured by spreading one loopful from each dilution onto the agar plates and visually determining the lowest concentration of RTIL that supported no colony formation. The MIC of both RTILs was 30 µM. The MBC of the RTILs deviated slightly from one another. The MBC of C_{16}MIMBr was 100 µM and the MBC of C_{14}OCMIMCl was 70 µM.

The antibacterial activities of C_{16}MIM-MSN and C_{14}OCMIM-MSN were measured by series dilution for 24 h at 25 °C and 48 h at 37 °C as shown in Figure 6a and b, respectively. The two MSNs were suspended in 6 mL of tryptic soy broth with 0.6% yeast extract and inoculated with 1 mL of 18 hour stock culture of *E. coli K12*. At various times, aliquots of each sample were diluted and plated on tryptic soy agar with 0.6% yeast extract. The plates were incubated for 18 h. Colonies were counted and recorded for dilutions containing between 30 and 300 colonies. In contrast to the similar MBC values for the free RTILs, C_{16}MIM-MSN exhibited a superior antibacterial activity than that of C_{14}OCMIM-MSN by a thousand fold. The diffusion of both RTIL from the pores slowed down at 25 °C. The pronounced difference in antibacterial activity between the two RTIL-MSN materials could be attributed to the different release profiles of the pore-encapsulated RTIL molecules. According to the aforementioned TEM analyses, the pore morphologies of these two samples are very different. C_{16}MIM-MSN has a hexagonal array ordered pores that all line up parallel, while C_{14}OCMIM-MSN has a disordered pore arrangement. It is plausible that the rate of RTIL release via diffusion from the parallel hexagonal channels of C_{16}MIM-MSN would be faster than that of the disordered pores of C_{14}OCMIM-MSN. In addition to pore morphology, the mass transfer of RTIL from the tubular particles (C_{14}OCMIM-MSN) will be considerably slower than the spherical particle (C_{16}MIM-MSN). The antibacterial activity of as-synthesized MCM-41 synthesized with conventional methods (CTAB as template) was measured by the same method and found to have similar activity as C_{16}MIM-MSN (see Supporting Information Figure S1).

The dependence of ionic strength on template release was measured by ^{1}H NMR. It seems that there is a base 10 log dependence of ionic strength on the template release.

In conclusion, we have demonstrated that the particle and pore morphology of mesoporous silica nanoparticle materials could be tuned by using various room temperature ionic liquids as synthetic templates. The antibacterial activities of two RTIL-MSNs have been measured against *E. coli K12*. The antibacterial activity was dependent on the rate of diffusional release of the pore-encapsulated RTIL, which was governed by the particle and pore morphology of the MSN materials. By further functionalizing the surface of these RTIL-MSN materials with various organic moieties, we envision that these materials could serve as a new generation of controlled release delivery nanodevices for various applications.

ACKNOWLEDGMENT. This research was supported by NSF (CHE-0239570). The authors thank Dr. M. J. Kramer and Dr. L. S. Chumbley for experimental assistance in TEM measurements of the materials and helpful discussions.

REFERENCES

(1) (a) Beck, J. S.; Vartuli, J. C.; Roth, W. J.; Leonowicz, M. E.; Kresge, C. T.; Schmitt, K. D.; Chu, C. T. W.; Olson, D. H.; Sheppard, E. W. *J. Am. Chem. Soc.* **1992**, *114*, 10834-10843. (b) Kresge, C. T.; Leonowicz, M. E.; Roth, W. J.; Vartuli, J. C.; Beck, J. S. *Nature (London)* **1992**, *359*, 710-712.

(2) Zhao, D.; Feng, J.; Huo, Q.; Melosh, N.; Frederickson, G. H.; Chmelka, B. F.; Stucky, G. D. *Science (Washington, D. C.)* **1998**, *279*, 548-552.

(3) Bagshaw, S. A.; Prouzet, E.; Pinnavaia, T. J. *Science (Washington, D. C.)* **1995**, *269*, 1242-1244.

(4) Ryoo, R.; Kim, J. M.; Ko, C. H.; Shin, C. H. *J. Phys. Chem.* **1996**, *100*, 17718-17721.

(5) Inagaki, S.; Koiwai, A.; Suzuki, N.; Fukushima, Y.; Kuroda, K. *Bull. Chem. Soc. Jpn.* **1996**, *69*, 1449-1457.

(6) (a) Lin, V. S. Y.; Lai, C.-Y.; Huang, J.; Song, S.-A.; Xu, S. *J. Am. Chem. Soc.* **2001**, *123*, 11510-11511. (b) Radu, D. R.; Lai, C.-Y.; Wiench, J. W.; Pruski, M.; Lin, V. S. Y. *J. Am. Chem. Soc.* **2004**, *126*, 1640-1641. (c)

Casasus, R.; Marcos, M. D.; Martinez-Manez, R.; Ros-Lis, J. V.; Soto, J.; Villaescusa, L. A.; Amoros, P.; Beltran, D.; Guillem, C.; Latorre, J. *J. Am. Chem. Soc.* **2004**, *126*, 8612-8613.

(7) (a) Huh, S.; Chen, H.-T.; Wiench, J. W.; Pruski, M.; Lin, V. S. Y. *J. Am. Chem. Soc.* **2004**, *126*, 1010-1011. (b) Lin, V. S. Y.; Radu, D. R.; Han, M.-K.; Deng, W.; Kuroki, S.; Shanks, B. H.; Pruski, M. *J. Am. Chem. Soc.* **2002**, *124*, 9040-9041. (c) Corma, A. *Chem. Rev.* **1997**, *97*, 2373-2419 and references therein. (d) Thomas, J. M. *J. Mol. Catal. A* **1999**, *146*, 77-85. (e) Brunel, D.; Blanc, A. C.; Galarneau, A.; Fajula, F. *Catal. Today* **2002**, *73*, 139-152.

(8) (a) Lai, C.-Y.; Trewyn, B. G.; Jeftinija, D. M.; Jeftinija, K.; Xu, S.; Jeftinija, S.; Lin, V. S. Y. *J. Am. Chem. Soc.* **2003**, *125*, 4451-4459. (b) Mal, N. K.; Fujiwara, M.; Tanaka, Y.; Taguchi, T.; Matsukata, M. *Chem. Mater.* **2003**, *15*, 3385-3394. (c) Vallet-Regi, M.; Ramila, A.; del Real, R. P.; Perez-Pariente, J. *Chem. Mater.* **2001**, *13*, 308-311. (d) Tourne-Peteilh, C.; Brunel, D.; Begu, S.; Chiche, B.; Fajula, F.; Lerner, D. A.; Devoisselle, J.-M. *New J. Chem.* **2003**, *27*, 1415-1418.

(9) (a) Huh, S.; Wiench, J. W.; Yoo, J.-C.; Pruski, M.; Lin, V. S. Y. *Chem. Mater.* **2003**, *15*, 4247-4256. (b) Huh, S.; Wiench, J. W.; Trewyn, B. G.; Song, S.; Pruski, M.; Lin, V. S. Y. *Chem. Commun. (Cambridge)* **2003**, 2364-2365.

(10) (a) Zhou, Y.; Antonietti, M. *Adv. Mater. (Weinheim, Ger.)* **2003**, *15*, 1452-1455. (b) Zhou, Y.; Schattka, J. H.; Antonietti, M. *Nano Lett.* **2004**, *4*, 477-481. (c) Zhou, Y.; Antonietti, M. *Chem. Mater.* **2004**, *16*, 544-550. (d) Lee, B.; Luo, H.; Yuan, C. Y.; Lin, J. S.; Dai, S. *Chem. Commun.* **2004**, 240-241.

(11) Pernak, J.; Sobaszkiewicz, K.; Mirska, I. *Green Chem.* **2003**, *5*, 52-56.

(12) Che, S.; Liu, Z.; Ohsuna, T.; Sakamoto, K.; Terasaki, O.; Tatsumi, T. *Nature (London)* **2004**, *429*, 281-284.

(13) Davis, B.; Jordan, P. An Overview of the Biocidal Activity of Cationics and Ampholities. In *Ind. Appl. Surfactants II;* Karsa, D. R., Ed.; Royal Society of Chemistry; Cambridge, 1990; Vol. 77, pp 195-210.

FIGURE CAPTIONS

Figure 1. Chemical structures of 1-tetradecyl-3-methylimidazolium bromide (C_{14}MIMBr), 1-hexadecyl-3-methylimidazolium bromide (C_{16}MIMBr), 1-octadecyl-3-methylimidazolium bromide (C_{18}MIMBr), and 1-tetradecyloxymethyl-3-methylimidazolium chloride (C_{14}OCMIMCl).

Figure 2. Schematic representation of the controlled release process of C_nMIM-MSN and its antibacterial activity against *E. coli*.

Figure 3. Transmission electron micrographs of C_nMIM-MSN materials. **(a)** C_{14}MIM-MSN, **(b)** C_{16}MIM-MSN, **(c)** C_{18}MIM-MSN, and **(d)** C_{14}OCMIM-MSN. These micrographs were obtained from a Phillips CM30 TEM operated at 300 kV.

Figure 4. Low angle powder X-ray diffraction patterns of RTIL-removed C_nMIM-MSN materials. **(a)** C_{14}MIM-MSN, **(b)** C_{16}MIM-MSN, **(c)** C_{18}MIM-MSN, and **(d)** C_{14}OCMIM-MSN. The diffraction data were collected on a Scintag XRD 2000 X-ray diffractometer using Cu Kα radiation. The

samples were scanned from 1.5° to 10° (2θ) with a step size of 0.02° and a count time of 0.5 s at each point.

Figure 5. Disk diffusion assay of 15 mM C_{16}MIM-MSN **(a)**, C_{14}OCMIM-MSN **(b)**, and phosphate buffer **(c)** on a lawn of *E. coli K12.* The red arrow points to an area of microbial lawn and the blue arrow points to the zone of clearing caused by the diffusion of RTIL.

Figure 6. Histogram of the antibacterial activity of C_nMIM-MSNs against *E. coli K12* at 25 °C **(a)** and 37 °C **(b)**. Four samples were measured at each temperature: C_{16}MIM-MSN (black bars), C_{14}OCMIM-MSN (green bars), RTIL-removed C_{16}MIM-MSN (blue bars), and blank control (no silica material) (red bars).

Table 1. Nitrogen sorption data of C_nMIM-MSN material.

	BET surface area (m^2/g)	Pore volume (cm^3/g)	BJH Average Pore Diameter (Å)
$C_{14}MIM$-MSN	729	0.664	27.1
$C_{16}MIM$-MSN	924	0.950	30.3
$C_{18}MIM$-MSN	893	0.995	32.7
$C_{14}OCMIM$-MSN	639	0.695	26.1

Figure 1.

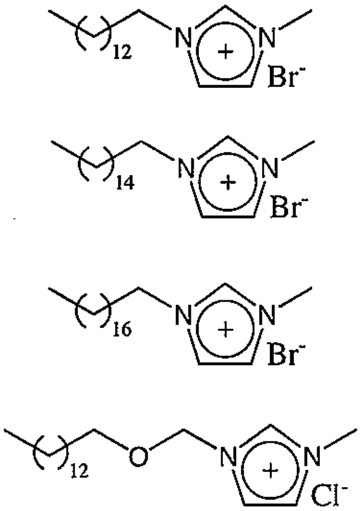

C_{14}MIMBr

C_{16}MIMBr

C_{18}MIMBr

C_{14}OCMIMCl

Figure 2.

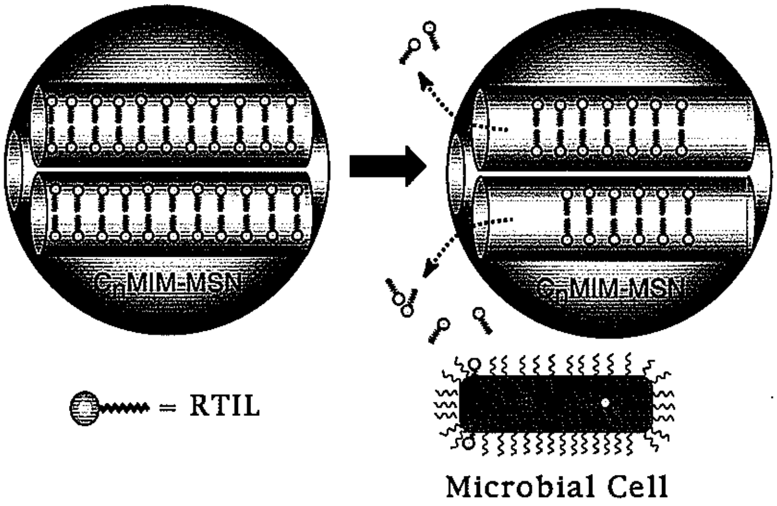

Figure 3.

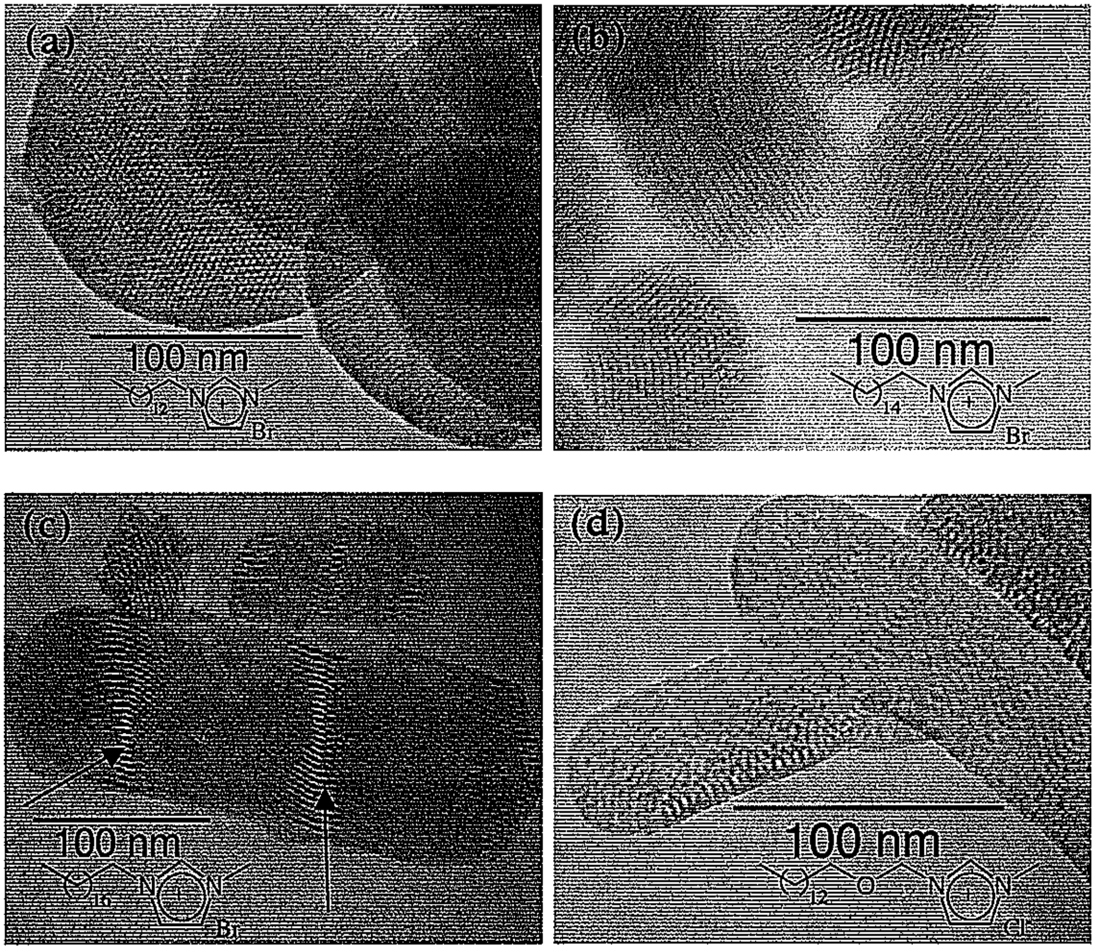

Figure 4.

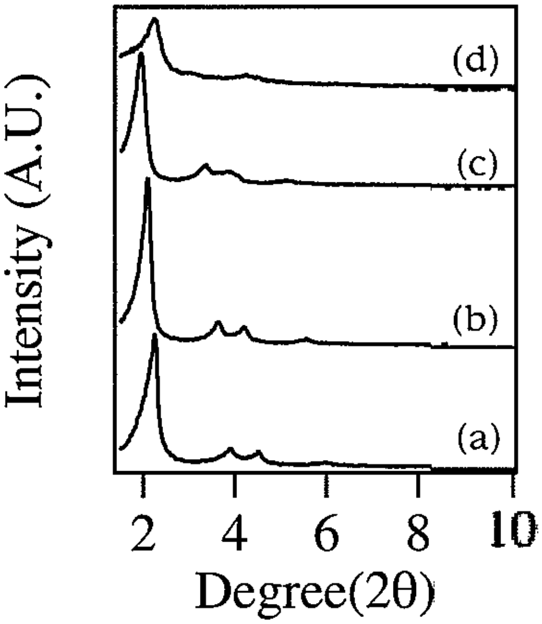

Figure 5.

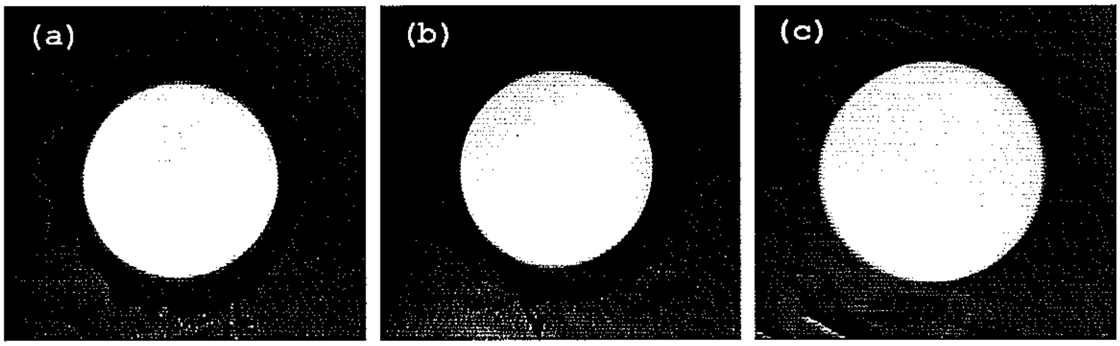

Figure 6.

(a)

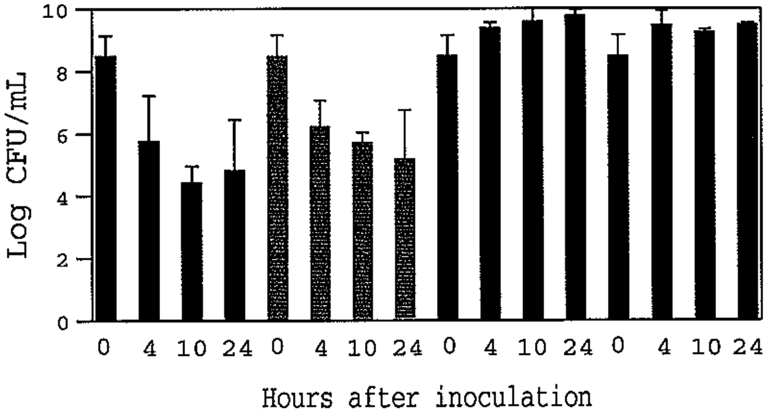
Log CFU/mL
0
2
4
6
8
10
0 4 10 24 0 4 10 24 0 4 10 24 0 4 10 24
Hours after inoculation

(b)

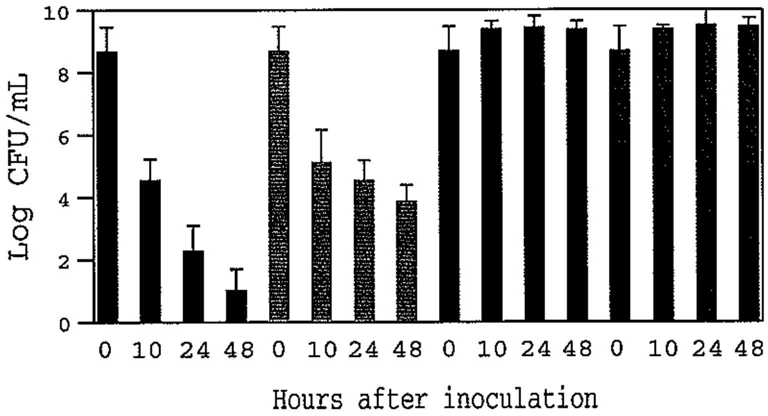
Log CFU/mL
0
2
4
6
8
10
0 10 24 48 0 10 24 48 0 10 24 48 0 10 24 48
Hours after inoculation

APPENDIX 1

Figure S1. Histogram of the antibacterial activity of CTAB-MSNs against *E. coli K12* at 37 °C. Two samples were measured: CTAB-MSN (black bars) and blank control (no silica material) (red bars).

Figure S2. Dependence ionic strength has on the release of RTIL from the pores of C_{16}MIM-MSN.

Figure S1.

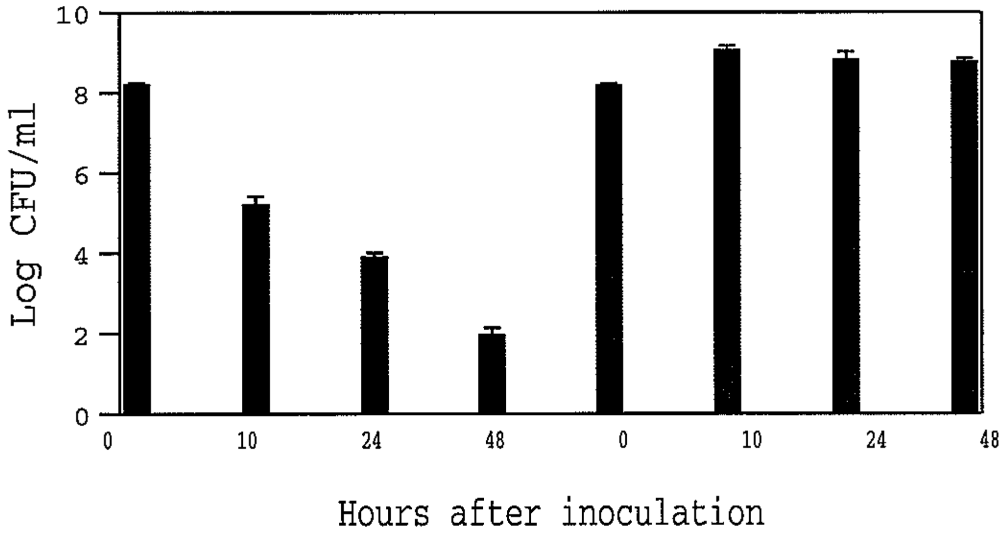
10
8
6
4
2
0
Log CFU/ml
0
10
24
48
0
10
24
48
Hours after inoculation

Figure S2.

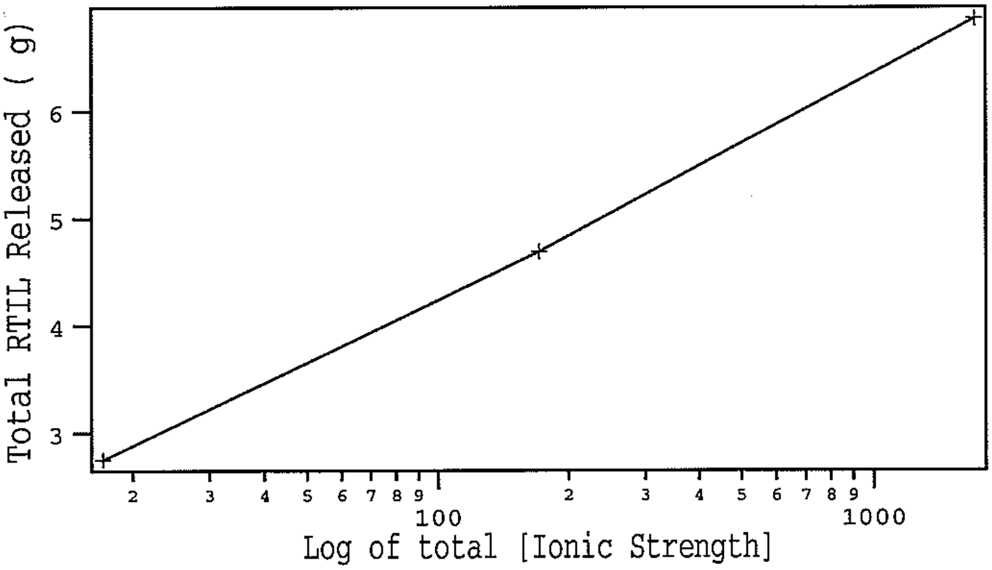
Total RTIL Released (g)
3
4
5
6
2
3
4
5
6
7
8
9
100
2
3
4
5
6
7
8
9
1000
Log of total [Ionic Strength]

CHAPTER 3. ENDOCYTOSIS OF TRI(ETHYLENE GLYCOL) FUNCTIONALIZED MESOPOROUS SILICA NANOPARTICLES INTO CANCER AND PLANT CELLS

Brian G. Trewyn, Francios Terney, Jennifer A. Nieweg, Joseph D. Buss, Kan Wang, and Victor S.-Y. Lin*

*Primary researcher and author

To be submitted to *NanoLetters*

ABSTRACT

The involvement of a specific organosiloxane functional group covalently attached to the exterior of fluorescein doped mesoporous silica nanoparticles on the degree and kinetics of endocytosis in cancer and plant cells was investigated. The kinetics of endocystosis of tri(ethylene glycol) functionalized fluorescein doped mesoporous silica nanoparticles (TEG coated FITC-MSNs) are significantly quicker than nonfunctional FITC-MSNs as determined by flow cytometry experiments. Fluorescence confocal microscopy investigation showed the endocytosis of TEG coated FITC-MSN into both HeLa cells and Tobacco protoplasts.

INTRODUCTION

In recent years, the use of mesoporous nanoparticles has spanned many divisions of the biological field, including sensors, drug delivery, and clinical diagnosis.[1-8] Mesoporous silica nanoparticles have many unique properties, such as an ordered pore structure, high surface area (~1000 m^2 g^{-1}), large pore volume (~0.9 cm^3 g^{-1}), tunable pore size with a narrow distribution (2.0-10 nm), and biocompatibility that makes them suitable for use in biological applications. Several active research groups have shown that mesoporous nanoparticles can act as reservoirs for drugs and biomolecules. Two groups have shown the ability to produce stimuli-responsive controlled release vehicles in MCM-41, both chemical and photocontrolled release were demonstrated.[4,8,9]

Concurrently, with the study of controlled release, the endocytosis of these mesoporous nanoparticles is being investigated. Endocytosis is the process of the internalization of molecules, particles, and nutrients from the plasma membrane and extracellular environment. It is an essential process of eukaryotic cells, which are cells that contain genetic DNA in the form of chromosomes within a distinct nucleus. Recent reports in the literature have demonstrated that mesoporous silica nanoparticles can undergo endocytosis into various animal cell types.[10-12] Mou and coworkers functionalized nanosized mesoporous silcas that, upon internalization, can be used as fluorescence cell tags.[12] With the ability of cell internalization and the fact that endocytosis and endocytic proteins are linked closely with human cancer,[13,14] research in this field is novel and important to study.

The study of endocytosis in higher order plants remained inactive for a long period of time because it was thought that plant endocytosis could not occur against the high turgor pressure in plant cells. However, recent publications contradict this former belief.[15-22] Volkmann and coworkers demonstrated the internalization of the fluorescent dye Lucifer Yellow presumably by endocytosis, as evidenced by light and electron microscopy.[23] Paciorek and coworkers demonstrated that auxin, a major regulator of plant development inhibits plant endocytosis.[24] Despite the doubts based on turgor pressure, endocytosis is possible in intact plant cells and evidence supporting this notion are continually being discovered.

In this paper, we functionalized mesoporous silica nanoparticles (MSNs), which were internalized by animal and plant cells. The fluorescein doped MSNs developed in our laboratory are easily prepared, and have strong fluorescence intensity, excellent photostability, and no fluorescein leaching.

EXPERIMENTAL SECTION

Reagents and Materials for Material Synthesis: Fluorescein isothiocyanate, isomer 1 (90%) (FITC), 3-aminopropyl-trimethoxysilane (97%) (APTMS), *n*-cetyltrimethylammonium bromide (CTAB), phosphorus tribromide (99%), pyridine, tri(ethylene glycol) monomethyl ether (95%) were all purchased from Aldrich and used as received. Tetraethoxysilane (TEOS) was purchased from Gelest and used as received.

Synthesis of Fluorescein-doped MSNs (FITC-MSN): The MSN material was prepared by the following procedures: First, 1.0 mg fluorescein isothiocyanate was stirred overnight at room temperature with 500 μL 3-aminopropyltrimethoxysilane (APTMS) in 500 μL anhydrous DMF. Next, n-cetyltrimethylammonium bromide (CTAB, 1.00 g, 2.74×10^{-3} mol) was dissolved in 480 mL nanopure water. This solution was made basic by the addition of 3.5 mL 2.00 M NaOH, followed by adjusting the solution temperature to 353 K. TEOS (5.00 mL, 2.57×10^{-3} mol) was first introduced dropwise to the template solution, followed by the dropwise addition of the FITC-APTMS/DMF solution. The mixture was stirred for 2 h at 353 K to give rise to orange precipitates (as synthesized FITC-MSNs). The solid product was filtered, washed with deionized water and methanol, and dried in under high vacuum at 353 K. To remove the surfactant template (CTAB), 1.0 g of as-synthesized FITC-MSNs were refluxed for 18 h in a solution of 1.0 mL of HCl (37.4%) and 100.0 mL of methanol, followed by washing with methanol and water. The yellow surfactant removed FITC-MSNs (washed FITC-MSNs) were placed under high vacuum to remove solvent from the mesopores.

Synthesis of Tri(ethylene glycol) Trimethoxysilane Molecules (TEG): This molecule was synthesized by a modified technique developed by Zheng et. al.[25] Phosphorous tribromide (9.0 g, 3.3×10^{-2} mol) was added dropwise to a stirred mixture of tri(ethylene glycol) monomethyl ether (7.7 g, 4.8×10^{-2} mol) and pyridine (2.0 g, 2.5×10^{-2} mol) at 0°C. The orange solution was stirred at room temperature for 48 h. Reaction was quenched with 10 mL water, and the product was extracted three times with 40 mL carbon tetrachloride. The combined organic extracts were washed successively with 25 mL of each 10% sodium carbonate, 5% sulfuric acid, and water, followed by drying with anhydrous magnesium sulfate. The carbon tetrachloride was removed under reduced pressure and the crude product was dried under high vacuum. The crude product (2.7 g) was dissolved in 10 mL ethanol. While this was stirred, 3-aminopropyltrimethoxysilane (2.10 g, 1.17×10^{-2} mol) was added dropwise to form tri(ethylene glycol) propyltrimethoxysilane (EG_3TMS). This was heated for 24 h at 90 °C.

Synthesis of TEG coated Fluorescein-doped Mesoporous Silica Nanoparticles (TEG coated FITC-MSN): To coat the FITC-MSNs, 200 mg was first suspended in 20 mL chloroform by sonicating for 30 min. Following sonication, 220 mg EG_3TMS was dissolved in 5 mL chloroform and added to the suspension. The solution was refluxed for 24 h, after which the TEG-FITC MSNs were filtered, and washed with chloroform, methanol and water.

Instrumental Methods, Conditions, and Parameters for the Structure Characterizations of FITC-MSN and TEG-coated FITC MSN: Powder XRD diffraction data was collected on a Scintag XRD 2000 X-ray diffractometer using Cu Kα radiation. Nitrogen adsorption and desorption isotherms, surface areas, and median pore diameters were measured using a Micromeritics ASAP2000 sorptometer. Sample preparation included degassing at 90 °C for 6 h. Nitrogen adsoption and desorption isotherms of these materials were obtained at -196 °C. Specific surface areas and pore size distributions were calculated using the Brunauer-Emmett-Teller (BET) and Barrett-Joyner-Halenda (BJH) method, respectively. Particle morphology of these materials was determined by scanning electron microscopy (SEM) using a JEOL 840A scanning electron microscope with 20 kV accelerating voltage and 0.005 nA of beam current for imaging. For SEM analysis the sample was spread on a carbon stub and sputter coated with 20 Å of gold. For transmission electron microscopy (TEM) investigations, a small aliquot was suspended in methanol and a drop was placed on a lacey carbon film on a 400 mesh copper grid, the methanol was allowed to evaporate. The sample was examined with a Philips model CM-30 TEM operating at 300 kV.

Infrared spectroscopy was measured on a Nicolet Nexus 470 (Madison, WI), equipped with a cooled MCT/A detector and an Ever-Glo source. Omnic 5.2 software was used to collect the data and to perform data analysis. Dry air was purged through the optical bench to reduce IR absorbance due to water. Samples were prepared by mixing nanoparticles with KBr (~5% w/w).

For fluorescence confocal microscopy measurements, HeLa cells were grown on cover slips as reported below. Fluorescence confocal examinations were completed on a Leica TCS NT confocal microscope with UV, argon, and krypton lasers with excitation wavelengths at 340-458 nm, 488 nm, and 568 nm, respectively.

Reagents and Materials for Biological Studies: Human cervical cancer (HeLa), Chinese Hamster Ovarian (CHO) and Human vascular Endothelium cell lines were obtained from American Tissue Culture Collection (ATCC). Formaldehyde solution (37% w/w) was purchased from Fisher. 4,6-diamidino-2-phenylindole, dihydrochloride (DAPI) and trypan blue were purchased from Sigma-Aldrich. Trypsin (1x, 0.25%) in 0.1% EDTA—2Na without calcium and magnesium was purchased from Fisher Scientific.

Cell Line Maintenance: HeLa and CHO cells were maintained in T75 flasks using DMEM (Dulbucco's modified Eagle's medium) supplemented with 10% equine serum, 2 mM L-glutamine, 100 U mL^{-1} penicillin, 100 mg mL^{-1} streptomycin, and 1 mg mL^{-1} gentamycin. HeLa and CHO cells were split every 2-3 days. Endothelial cells were maintained in T75 flasks using Kaighn's F12K medium supplemented with 0.1 mg mL^{-1} heparin, 0.04 mg mL^{-1} endothelial cell growth supplement (ECGS), and 10% fetal bovine serum. Endothelial cells were split every 7-10 days.

Measuring the Dosage of FITC-MSN and TEG-coated FITC-MSN: To investigate the maximum amount of material that can be incorporated by HeLa and CHO cells, a dosage experiment was designed. The cells were grown in 6-well plates for 24, hours or until visual confluency developed; the cells were then treated with incremental amounts of FITC-MSNs and TEG-coated FITC-MSNs suspended in media. Experiments were designed for both FITC-MSNs and TEG coated FITC-MSNs with concentrations of 0, 0.01, 0.05, 0.10, 0.15, and 0.20 mg mL^{-1}. The cells were incubated with the varying concentrations of MSNs for 12 h at 37 °C in 5% CO_2. After 12 h, the cells were washed two times with PBS (phosphate-buffered saline) and trypsinized. The cells were incubated in 830 mM trypan blue for 10 min to quench the fluorescence of any MSNs adhered to the exterior of the cells. The MSN uptake was measured by flow cytometry.

Measuring the Kinetics of FITC-MSN and TEG-coated FITC-MSN Uptake: To investigate the rate of MSN uptake into HeLa and CHO cells, a kinetic experiment study was concieved.

The cells were grown in 6-well plates for 24 h, or until visual confluency developed. The cells were incubated with a uniform amount of MSNs (0.10 mg mL^{-1}) for varying amounts of time. Uptake was measured at 0, 0.5, 1.0, 1.5, 2.0, 4.0, and 6.0 time intervals. After the pre-determined amount of time, the cells were washed twice with PBS, and incubated in standard growth media. Fourteen hours after initial inoculation, the cells were trypsinized, and the MSN uptake was measured by flow cytometry.

Fluorescence Confocal Microscopy Measurements: To visually investigate the endocytosis of FITC-MSNs and TEG-coated FITC-MSNs, fluorescence confocal microscopy was employed. Coverslips (22 mm^2) were cleaned with 1 M HCl, nanopure water (3x), 50% ethanol, 70% ethanol, and 100% ethanol, and dried overnight at 60 °C. Following cleaning, the coverslips were placed on the bottom of the wells of 6-well plates and covered with 3 mL of standard growth media. HeLa and CHO cells (1×10^5 cells mL^{-1}) were grown for 24 h on the coverslips. After 24 h, the cells were inoculated with 0.1 mg mL^{-1} MSNs, and grown for an additional 12 h. Afterwards, the growth media was removed, the cells were washed with PBS (2x), and the cells were then reincubated with a PBS solution of 3.7% formaldehyde and 57 mM DAPI for

30 min. These coverslips were removed from the PBS solution and fixed to glass slides with liquid adesive.

Tobacco Protoplasts Isolation: *Nicotiana tabacum L.* cv. Petite Havana SR1 was grown aseptically on MS solid media for 6 weeks. Mesophyll protoplasts were isolated by modified processes previously described.[26] Briefly, pieces of tobacco leaves were incubated overnight at room temperature, in K4 medium with 1.2% cellulase Onozuka R-10 and 0.6% macerozyme R-10 under continuous gentle orbital shaking. After filtration, the digestion mixture was overlayed with W5 media and centrifuged for 15 minutes at 80g. The intact protoplasts form a ring at the interphase. Purified protoplasts were washed 3 times in W5 and adjusted to 1×10^6 cells mL^{-1}.

Protoplast Treatment: Protoplasts were incubated in W5 media with FITC-doped MSNs and TEG coated FITC-MSNs. The ratio used was 1×10^6 cell for 0.1 mg of MSN. The protoplasts were incubated in the dark, overnight at room temperate. After incubation, the protoplasts were separated from unincorporated MSN by centrifugation on a K4 medium cushion for 15 minutes at 80g.

Protoplasts Confocal Microscopy: All cells were observed alive with a Leica TCS/NT confocal microscope. For FITC the

Ar laser for excitation (488nm) was used and Kr laser (568nm) for the TRITC. 10 μL of the purified protoplasts were mounted on a glass slide and covered with a coverslip. Autofluorescence of chlorophyll is visible in all channels.

RESULTS AND DISCUSSION

To prepare TEG functional MSNs for the endocytosis studies, (Figure 1) fluorescein doped MSNs were first synthesized via a modified synthesis of our previously published synthesis. The synthesis was modified by first synthesizing a trimethoxysilane derivatized fluorescein molecule. Following this, the fluorescein derivative was added to the MSNs during addition of the silica monomer. After the mesoporous materials were synthesized, the previously synthesized tri(ethylene glycol) propyltrimethoxysilane was grafted to the exterior of the MSNs via reflux in toluene. Once the ethylene glycol group was grafted to the exterior of the MSNs the surfactant was removed from the pores via hydrochloric acid wash.

The material was fully characterized after the synthesis was complete and prior to cell studies. As depicted in figure 2a, the spherical morphology and the hexagonal pore structure of the TEG-grafted MSNs is readily observable by scanning (a) and transmission (b) electron microscopy investigation (SEM and TEM, respectively). The arrows in figure 2b point to the pores formed during the synthesis of the FITC-doped MSNs. Clearly the addition of the TEG-TMS did not change the particle or pore morphology.

The nitrogen adsorption/desorption isotherms are further evidence for MCM-41 type material with a typical BET isotherm (type IV) (Figure 3a). The surface area of the material was determined to be 1048 m^2 g^{-1}, with an average pore diameter of 27.4 Å before the TEG-TMS was grafted onto the surface. After grafting, the surface area decreased to 712.7 m^2 g^{-1} with an average pore diameter below 20 Å. The pore size was determined by BJH calculation and had a narrow size distribution (Table 1 and Figure 3b).

The powder x-ray diffraction (XRD) demonstrated more conclusively the MCM-41 type porous structure. Before the TEG-TMS was grafted, the hexagonal array of pores is easily distinguishable, as shown in the XRD in figure 4. Notice peaks representing the d_{100}, d_{110}, d_{200}, and d_{210} Miller indices are clearly present and labeled as such in figure 4a. After the TEG-TMS group was grafted some of the resolution was lost due to coverage of the organic functional groups. The d_{100} peak is still clearly present but decreased in intensity, again due to the presence of the TEG-TMS groups grafted to the exterior.

Finally, the evidence for the grafting of TEG-TMS was investigated by infrared spectroscopy (Figure 4b). Peaks are visible after the organic group was grafted above 2900 cm^{-1} (data not shown). These peaks represent C-H bond stretches and are not present before grafting.

Following complete material characterization, the interaction of the TEG coated FITC-MSNs with biological systems was investigated and compared to that of the uncoated FITC-MSNs. First, the uptake of both MSNs was measured as a function of the concentration in both CHO (Chinese Hamster Ovarian cancer) and HeLa (Human Cervical Cancer) cells. Endocytosis is staturated (>95%) for both cell lines with the addition of just 0.05 mg mL^{-1} TEG coated FITC-MSNs (Figures 5 & 6). At the same concentration, FITC- MSNs showed endocytosis of only ~10—15% into the cells. Following the dosage dependent study, the kinetics of endocytosis was measured in both cell lines. The rate at which cell internalization occurred for the TEG coated FITC-MSN exceeded that of the FITC-MSN by a significant amount for both cell lines (Figure 7 & 8). After just 30 minutes, over 90% of the recorded cells contained TEG coated FITC-MSNs, while just 5–7% of the cells internalized the FITC-MSNs.

Fluorescence confocal images showed that the TEG coated FITC-MSNs crossed the cell membrane and were internalized into the cells, most likely through endocytosis (Figure 9a-c). The green fluorescence of the fluorescien can be seen in the cytoplasm especially around the nucleus upon excitation at 494 nm (Figure 9a). To visualize the locations of the nuclei, the cells were excited at 358 nm (Figure 9b). The appearance of healthy intact nuclei and the visibility of fully grown cells by pseudo-brightfield suggested that the TEG coated FITC-MSN are biocompatible with HeLa cells under experimental conditions (Figure 9c). A series of fluorescence images of different cross-sections of TEG coated FITC-MSN containing HeLa cells were obtained by changing the focal depth by 1.2 μm vertically (Figure 10a-f).

Finally, the TEG coated FITC-MSNs were internalized by tobacco protoplasts (Figure 11a-l). The arrows indicate a cluster of TEG coated FITC-MSNs that are excited by the Ar laser. The round artifacts clustered just inside the protoplast are chloroplasts, and are excited at 488 nm and 568 nm by Ar and Kr lasers, respectively. In contrast, the

TEG coated FITC-MSNs are not visible when excited at 568 nm, which allows for the differentation of the nanoparticles from the chloroplasts. The nanoparticles without the organic functionality were not internalized by the tobacco protoplasts.

The mechanism by which the tri(ethylene glycol) functional group increases the cellular internalization ability is not completely clear. However, a recent publication and personal experimental observations gives some theories. To begin with, the ethylene glycol is a very hydrophilic molecule and, as observed in our laboratory, make the MSN suspend in aqueous solution for a much longer time and at a wider range of temperatures than non-functional MSN. In 2003, it was reported that tetra(ethylene glycol) protected gold nanoparticles had great stability in aqueous solutions with a high concentration of electrolytes. It was also reported that these gold nanoparticles with hydrophilic surfaces have complete resistance to protein nonspecific interactions.[25] This prevention of nonspecific protein interaction, plus the increased suspension stability, may be the reasons for increased cell uptake.

In summary, tri(ethylene glycol) functionalized fluorescein doped mesoporous silica nanoparticles were synthesized and extensively characterized. Internalization of the nanoparticles into HeLa and CHO cells, and accumulation in the cytoplasm was demonstrated. For the first time, the internalization of mesoporous silica nanoparticles was demonstrated in protoplasts. The MSNs appear to have no cytotoxic effects on both, animal and plant cell types.

FIGURE LEGENDS

Table 1.	Nitrogen sorption data of FITC-MSN and TEG coated FITC-MSN.
Figure 1.	Schematic representation of the TEG coated FITC doped MSNs, used to measure endocytosis into cancer and plant cells.
Figure 2.	Electron micrographs of TEG coated FITC doped MSNs: **(a)** Scanning electron micrographs **(b)** Transmission electron micrographs.
Figure 3.	**(a)** BET isotherm of surfactant-removed FITC-doped MSNs (red) and TEG grafted FITC-doped MSNs (blue). **(b)** BJH pore diameter distribution of surfactant-removed FITC-doped MSNs (red) and TEG grafted FITC-doped MSNs (blue).
Figure 4.	XRD spectra of surfactant-removed FITC-doped MSNs **(a)** and TEG grafted FITC-doped MSNs **(b)**.

Figure 5. Uptake of FITC-doped MSNs **(a)** and TEG grafted FITC doped MSNs **(b)** by HeLa cells after 12 h incubation at 37 °C as a function of nanoparticle concentration.

Figure 6. Uptake of FITC-doped MSNs **(a)** and TEG grafted FITC doped MSNs **(b)** by CHO cells after 12 h incubation at 37 °C as a function of nanoparticle concentration.

Figure 7. Uptake of FITC-doped MSNs **(a)** and TEG grafted FITC doped MSNs **(b)** by HeLa cells at 37 °C as a function of varying incubation time. The dosing concentration was 100 μg mL^{-1}.

Figure 8. Uptake of FITC-doped MSNs **(a)** and TEG grafted FITC doped MSNs **(b)** by CHO cells at 37 °C as a function of varying incubation time. The dosing concentration was 100 μg mL^{-1}.

Figure 9. Fluorescence confocal micrographs of HeLa cells incubated with 100 μg mL^{-1} of TEG coated FITC-doped MSNs for 12 h at 37 °C: **a.)** cells

excited in the UV region; **b.)** cells excited at 494 nm; **c.)** a pseudo-brightfield image.

Figure 10. Flourescence confocal micrographs of HeLa cells after 12 h incubation demonstrating endocytosis of TEG coated FITC-MSNs **(a)-(f)**. Each frame represents a focal point with 1.2 μm vertical difference.

Figure 11. Fluorescence confocal micrograph images of Tobacco protoplasts, demonstrating the endocytosis of TEG coated FITC-MSNs after incubation at room temperature overnight **(a)-(l)**.

Table one.

	BET surface area ($m^2\ g^{-1}$)	Pore volume ($cm^3\ g^{-1}$)	BJH Average Pore Diameter (Å)
FITC-MSN	1048	0.914	27.4
TEG coated FITC-MSN	713	0.367	≥20

FIGURES

Figure 1.

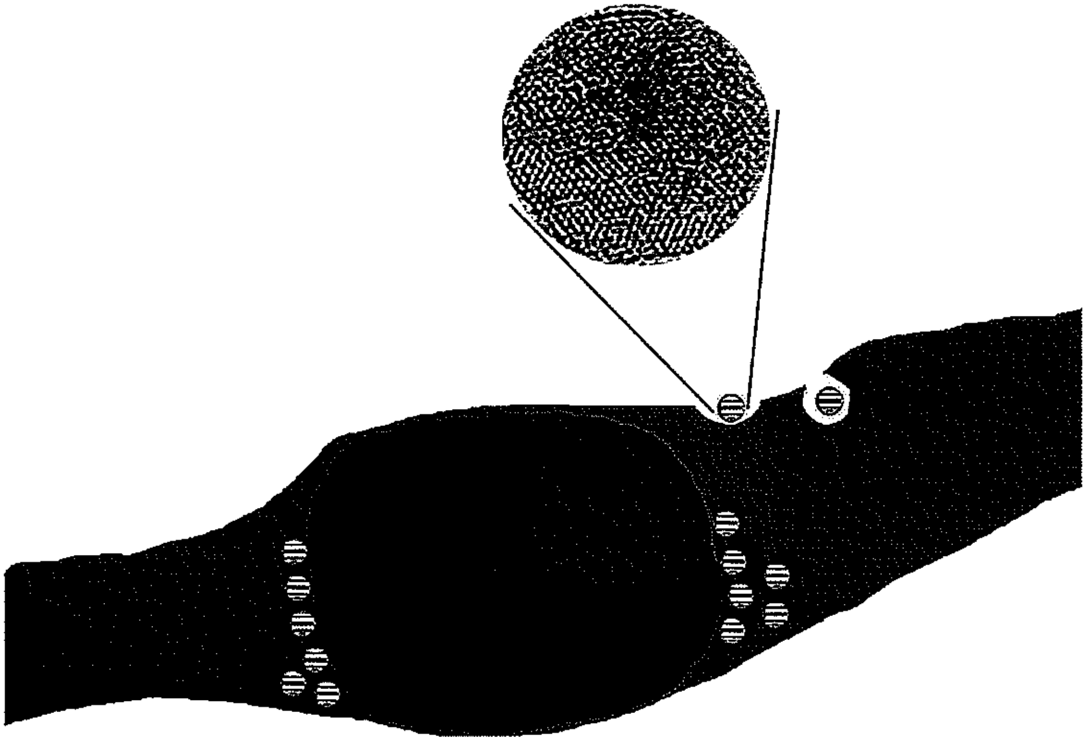

Figure 2a.

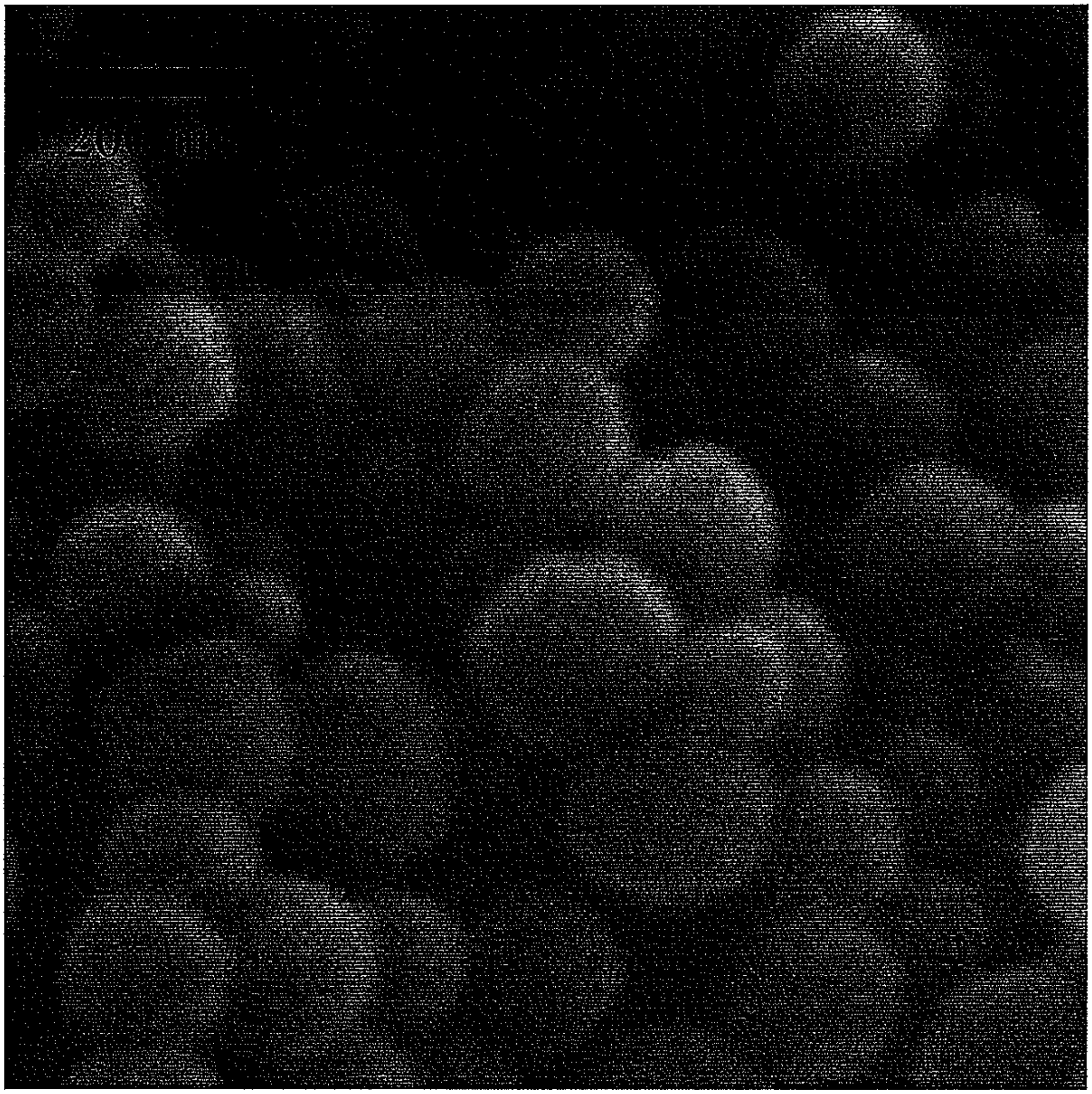

Figure 2b.

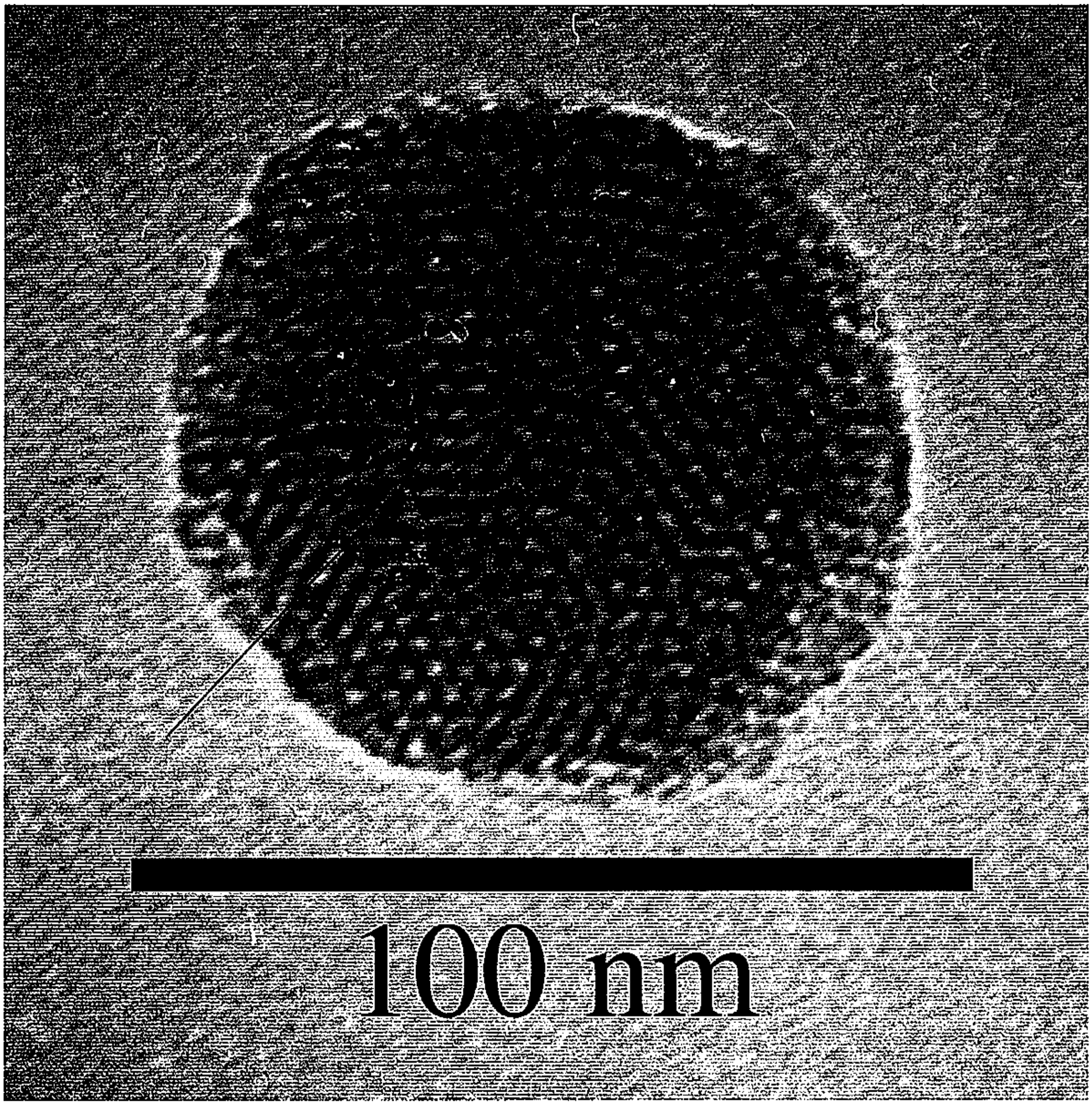

Figure 3.

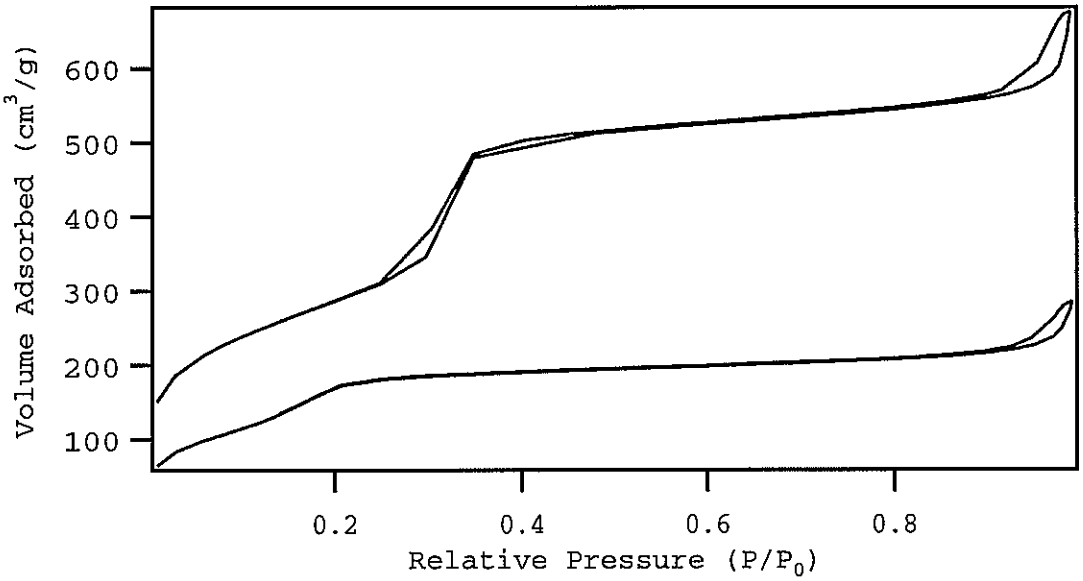
Volume Adsorbed (cm^3/g)
600
500
400
300
200
100
0.2
0.4
0.6
0.8
Relative Pressure (P/P$_0$)

Figure 3b.

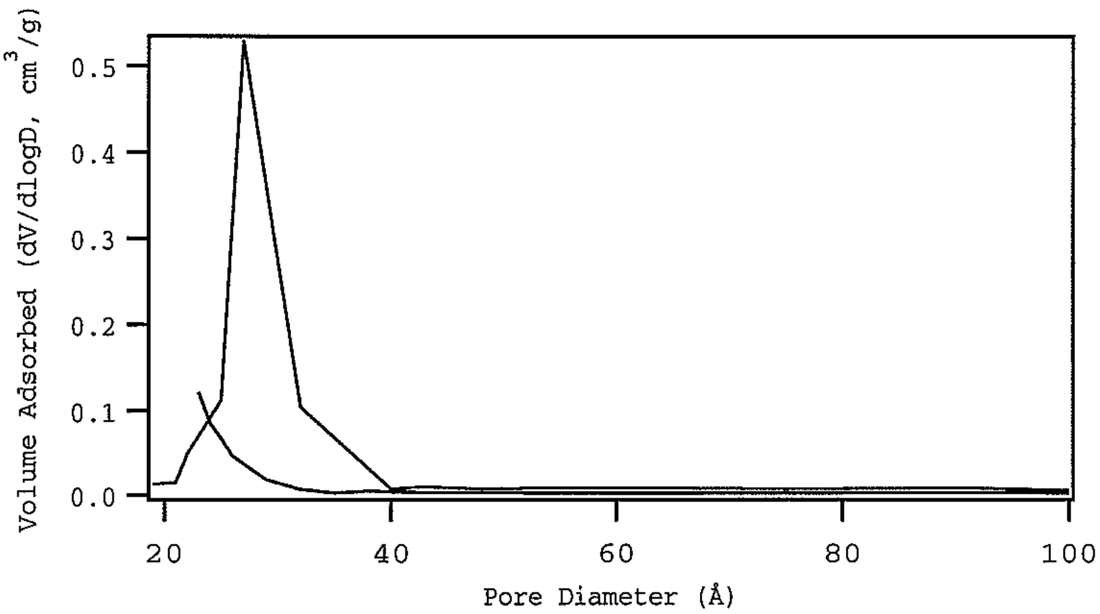
Volume Adsorbed (dV/dlogD, cm^3/g)
0.5
0.4
0.3
0.2
0.1
0.0
20
40
60
80
100
Pore Diameter (Å)

Figure 4.

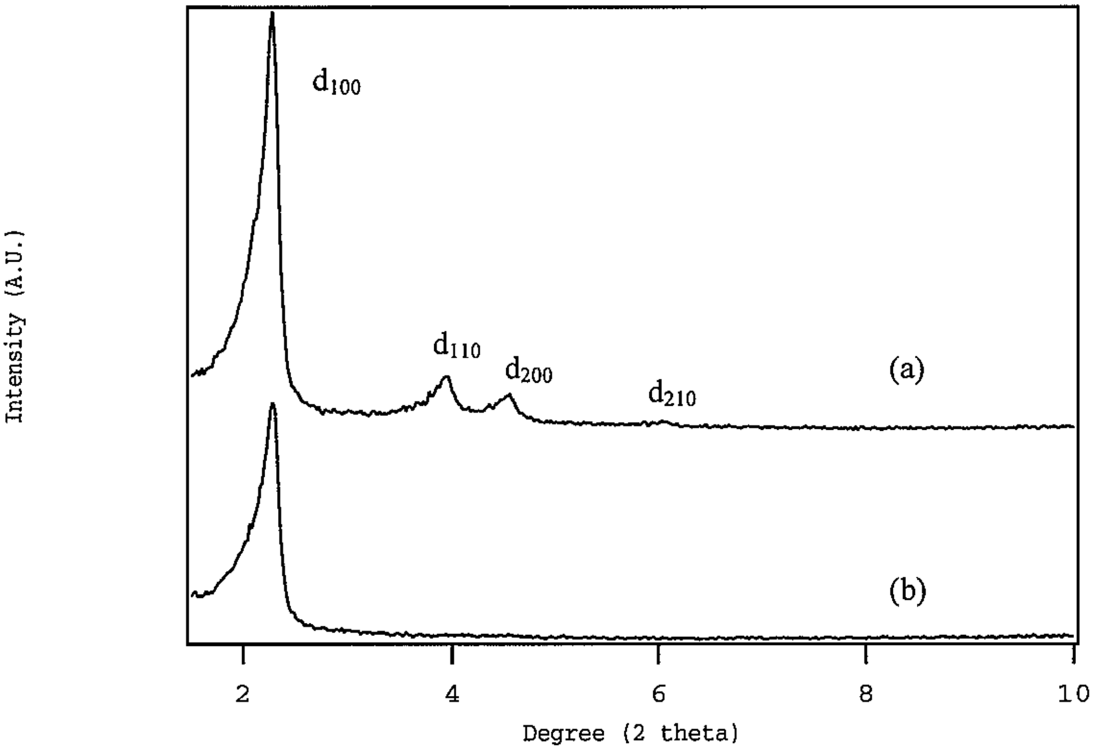

Figure 5.

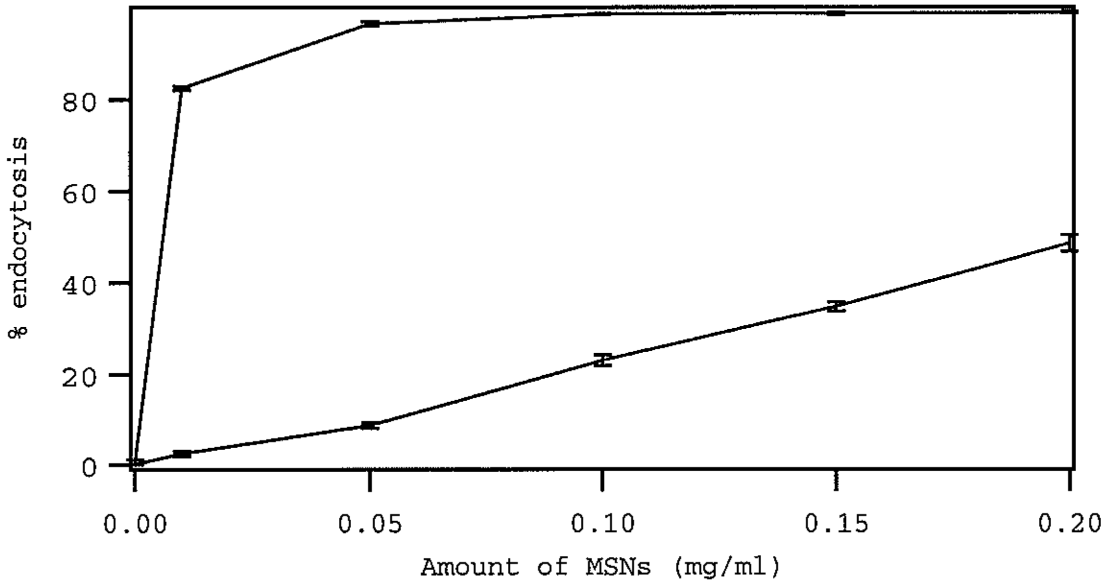
% endocytosis
0
20
40
60
80
0.00
0.05
0.10
0.15
0.20
Amount of MSNs (mg/ml)

Figure 6.

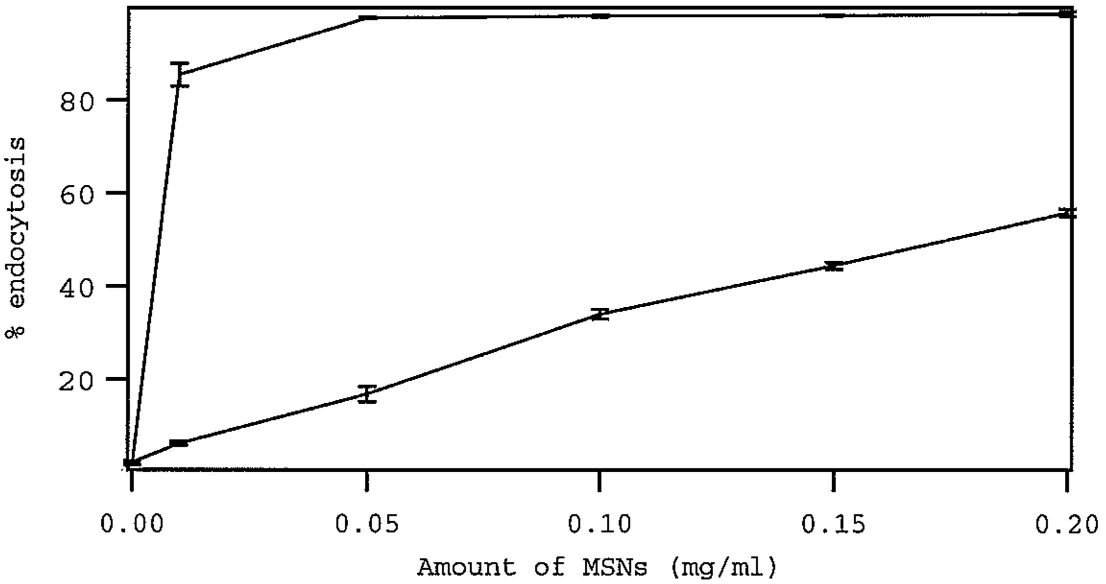

% endocytosis
80
60
40
20
0.00
0.05
0.10
0.15
0.20
Amount of MSNs (mg/ml)

Figure 7.

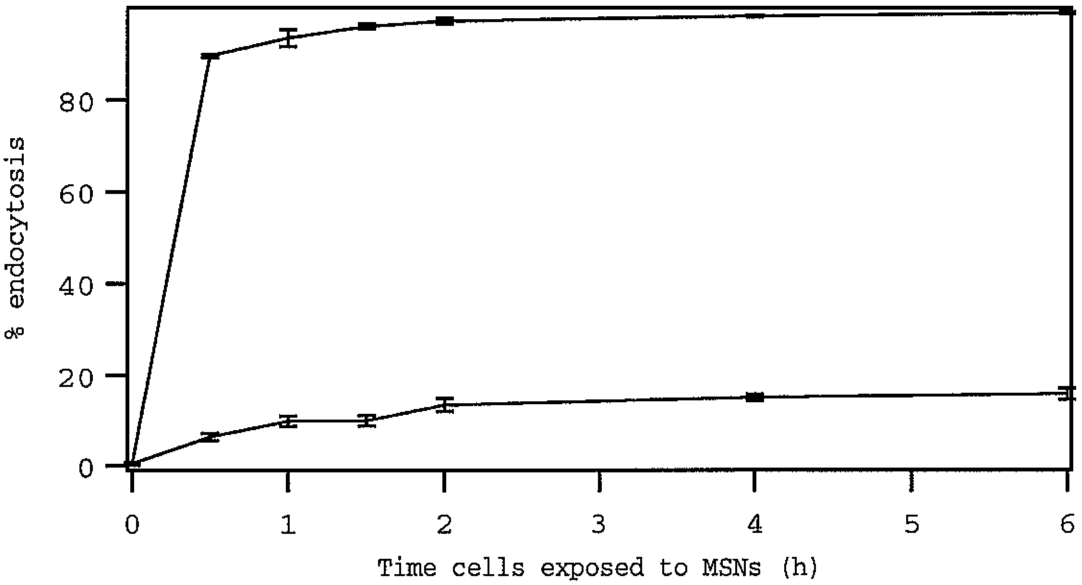
% endocytosis
0
20
40
60
80
0
1
2
3
4
5
6
Time cells exposed to MSNs (h)

Figure 8.

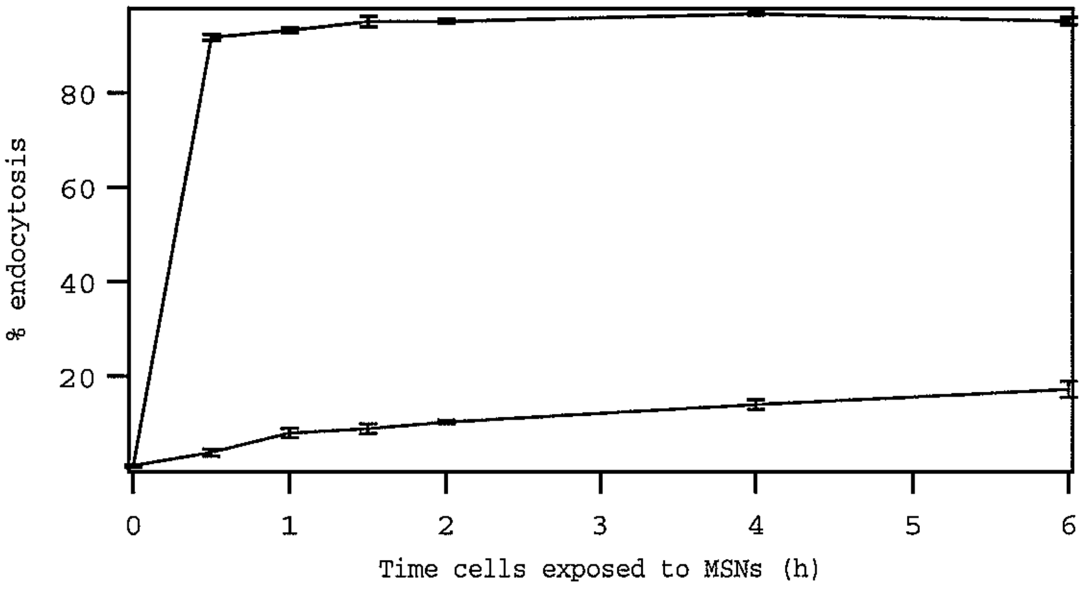

Figure 9.

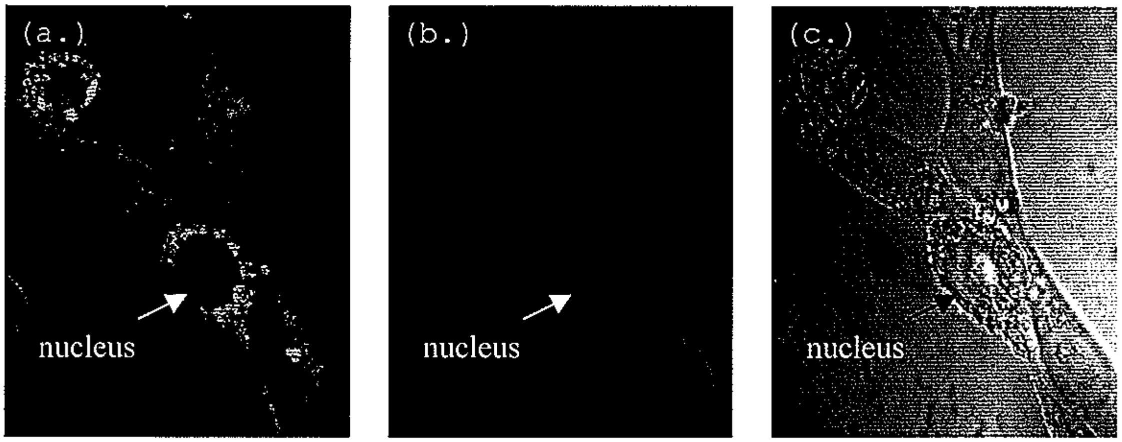

Figure 10.

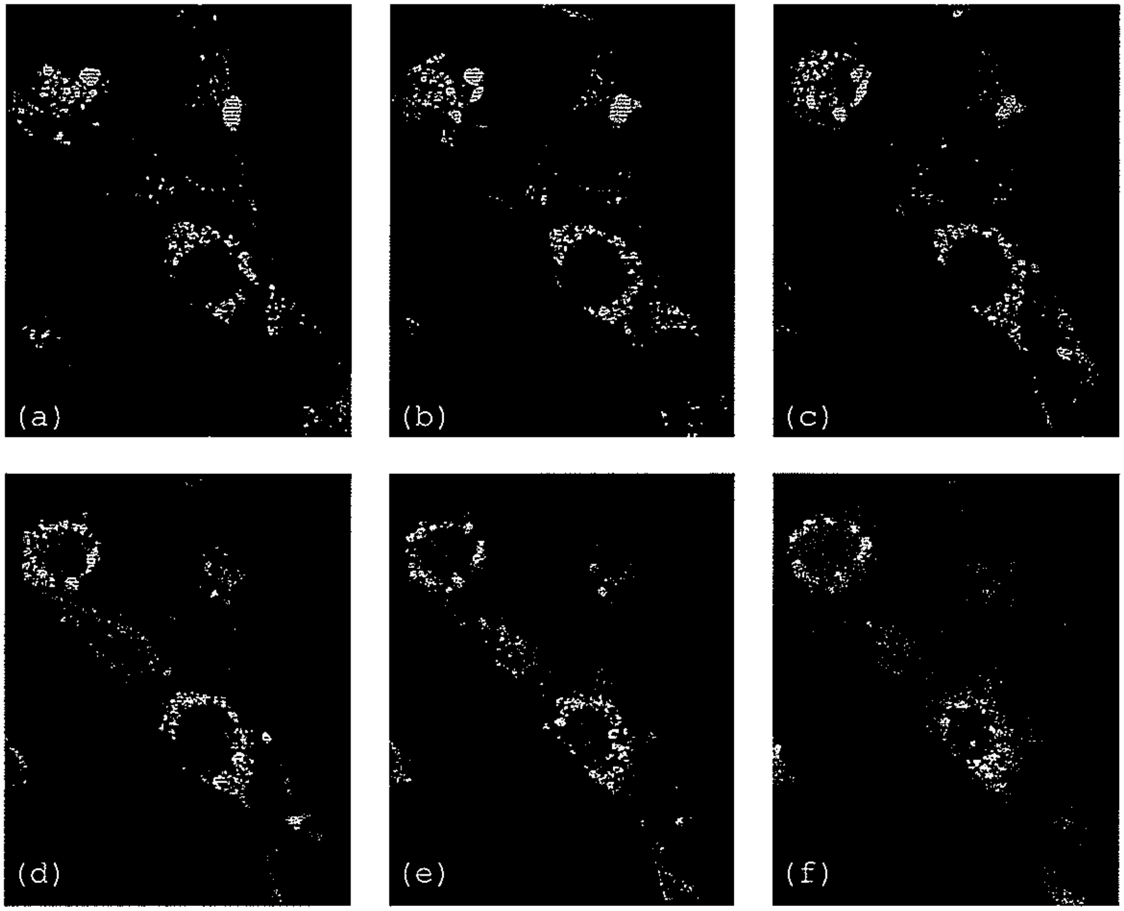

Figure 11.

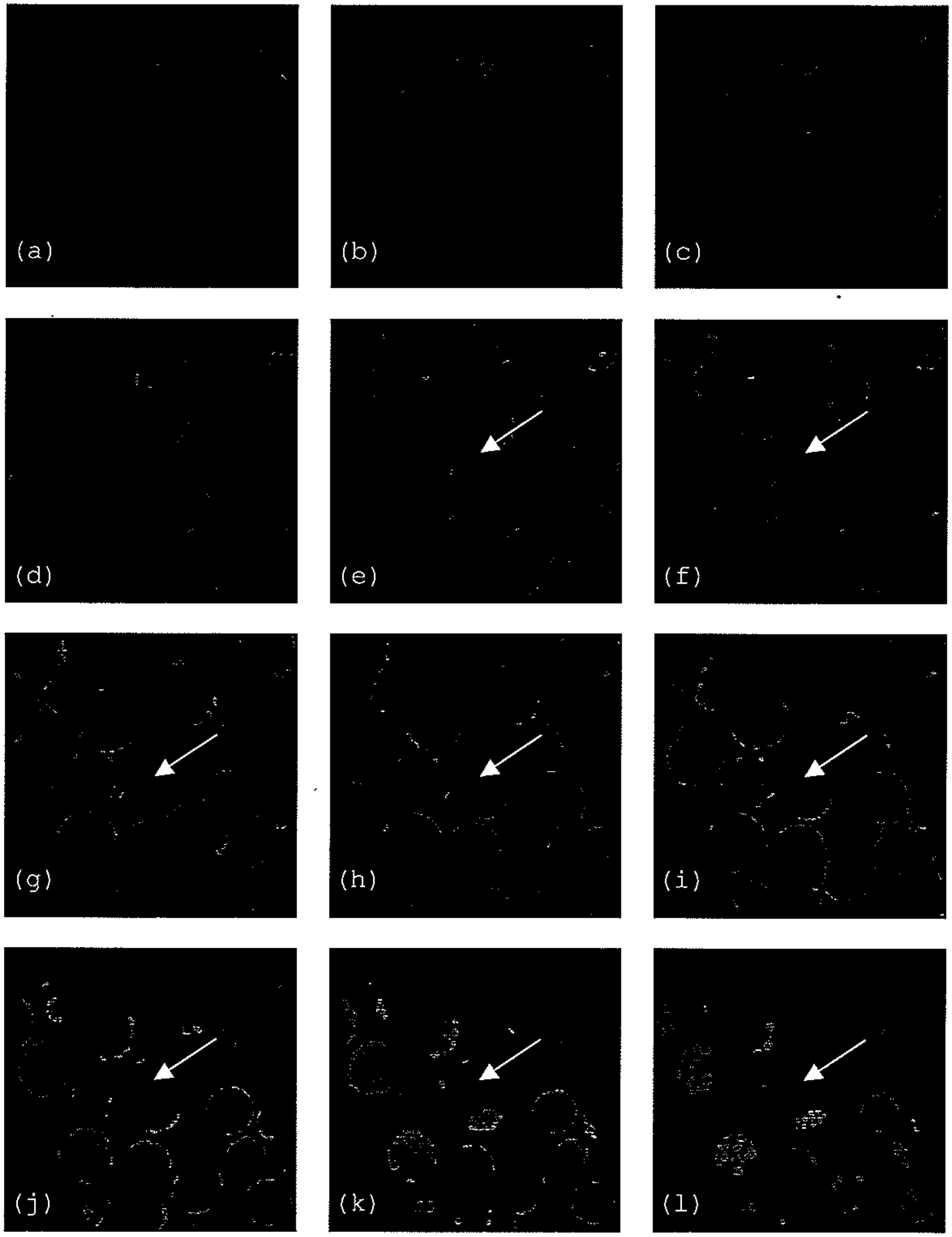

REFERENCES

(1) Descalzo, A. B.; Marcos, M. D.; Martinez-Manez, R.; Soto, J.; Beltran, D.; Amoros, P. *Journal of Materials Chemistry* **2005**, *15*, 2721-2731.

(2) Radu, D. R.; Lai, C.-Y.; Wiench, J. W.; Pruski, M.; Lin, V. S. Y. *Journal of the American Chemical Society* **2004**, *126*, 1640-1641.

(3) Andersson, J.; Rosenholm, J.; Areva, S.; Linden, M. *Chemistry of Materials* **2004**, *16*, 4160-4167.

(4) Mal, N. K.; Fujiwara, M.; Tanaka, Y. *Nature (London, United Kingdom)* **2003**, *421*, 350-353.

(5) Ostafin, A. E.; Burgess, J. P.; Mizukami, H. *Tissue Engineering and Novel Delivery Systems* **2004**, 483-503.

(6) Tozuka, Y.; Oguchi, T.; Yamamoto, K. *Pharmaceutical Research* **2003**, *20*, 926-930.

(7) Vallet-Regi, M.; Doadrio, J. C.; Doadrio, A. L.; Izquierdo-Barba, I.; Perez-Pariente, J. *Solid State Ionics* **2004**, *172*, 435-439.

(8) Lai, C.-Y.; Trewyn, B. G.; Jeftinija, D. M.; Jeftinija, K.; Xu, S.; Jeftinija, S.; Lin, V. S. Y. *Journal of the American Chemical Society* **2003**, *125*, 4451-4459.

(9) Giri, S.; Trewyn, B. G.; Stellmaker, M. P.; Lin, V. S. Y. *Angewandte Chemie, International Edition* **2005**, *44*, 5038-5044.

(10) Radu, D. R.; Lai, C.-Y.; Jeftinija, K.; Rowe, E. W.; Jeftinija, S.; Lin, V. S. Y. *Journal of the American Chemical Society* **2004**, *126*, 13216-13217.

(11) Huang, D.-M.; Hung, Y.; Ko, B.-S.; Hsu, S.-C.; Chen, W.-H.; Chien, C.-L.; Tsai, C.-P.; Kuo, C.-T.; Kang, J.-C.; Yang, C.-S.; Mou, C.-Y.; Chen, Y.-C. *FASEB Journal* **2005**, *19*, 2014-2016.

(12) Lin, Y.-S.; Tsai, C.-P.; Huang, H.-Y.; Kuo, C.-T.; Hung, Y.; Huang, D.-M.; Chen, Y.-C.; Mou, C.-Y. *Chemistry of Materials* **2005**, *17*, 4570-4573.

(13) Floyd, S.; De Camilli, P. *Trends in Cell Biology* **1998**, *8*, 299-301.

(14) Hyun, T. S.; Ross, T. S. *Trends in Molecular Medicine* **2004**, *10*, 194-199.

(15) Baluska, F.; Liners, F.; Hlavacka, A.; Schlicht, M.; Van Cutsem, P.; McCurdy, D. W.; Menzel, D. *Protoplasma* **2005**, *225*, 141-155.

(16) Baluska, F.; Samaj, J.; Hlavacka, A.; Kendrick-Jones, J.; Volkmann, D. *Journal of Experimental Botany* **2004**, *55*, 463-473.

(17) Dhonukshe, P.; Mathur, J.; Huelskamp, M.; Gadella, T. W. J., Jr. *BMC Biology* **2005**, *3*, No pp given.

(18) Etxeberria, E.; Baroja-Fernandez, E.; Munoz, F. J.; Pozueta-Romero, J. *Plant and Cell Physiology* **2005**, *46*, 474-481.

(19) Gross, A.; Kapp, D.; Nielsen, T.; Niehaus, K. *New Phytologist* **2005**, *165*, 215-226.

(20) Holstein, S. E. H. *Traffic (Oxford, United Kingdom)* **2002**, *3*, 614-620.

(21) Samaj, J.; Baluska, F.; Voigt, B.; Schlicht, M.; Volkmann, D.; Menzel, D. *Plant Physiology* **2004**, *135*, 1150-1161.

(22) Samaj, J.; Read, N. D.; Volkmann, D.; Menzel, D.; Baluska, F. *Trends in Cell Biology* **2005**, *15*, 425-433.

(23) Volkmann, D.; Mori, T.; Tirlapur, U. K.; Konig, K.; Fujiwara, T.; Kendrick-Jones, J.; Baluska, F. *Cell Biology International* **2003**, *27*, 289-291.

(24) Paciorek, T.; Zazimalova, E.; Ruthardt, N.; Petrasek, J.; Stierhof, Y.-D.; Kleine-Vehn, J.; Morris, D. A.; Emans, N.; Juergens, G.; Geldner, N.; Friml, J. *Nature (London, United Kingdom)* **2005**, *435*, 1251-1256.

(25) Zheng, M.; Davidson, F.; Huang, X. *Journal of the American Chemical Society* **2003**, *125*, 7790-7791.

(26) Spangenberg, G.; Osusky, M.; Oliveira, M. M.; Freydl, E.; Nagel, J.; Pais, M. S.; Potrykus, I. *Theoretical and Applied Genetics* **1990**, *80*, 577-87.

CHAPTER 4. TRANSMISSION ELECTRON MICROSCOPY AND *IN VITRO* INVESTIGATION OF FLUORESCEIN LOADED, IRON OXIDE NANOPARTICLE CAPPED MESOPOROUS SILICA NANOPARTICLES

*Brian G. Trewyn, Supratim Giri, Michael P. Stellmaker, and Victor S.-Y. Lin**

Published in Angew. Chem. Int. Ed. **2005**, *44,* 5038-5044.

ABSTRACT

Once the synthesis of a controlled-release delivery system based on MCM-41-type mesoporous silica nanorods capped with superparamagnetic iron oxide nanoparticles was completed, the material characterized, and the dosage and kinetics of the antioxidant dependent release; the biological interaction of the material was determined along with TEM measurements. The electron microscopy investigation proved the pore openings of the MSN were indeed blocked by the Fe_3O_4 nanoparticles. The biological interaction investigation demonstrated Fe_3O_4-capped MSN endocytosis into HeLa cells. Not only do the material enter the cells through endocytosis but it seems the fluorescein was released from the pores, most probably

caused by disulfide bond reducing molecules, antioxidants. In addition to endocytosis and release, the Fe_3O_4-capped MSN propelled the cells across a cuvette upon induction of a magnet force.

INTRODUCTION

While recent reports on surface-functionalized, superparamagnetic iron oxide nanoparticles have demonstrated their ability in drug/gene delivery,[1-3] magnetic resonance imaging,[4] thermal tumor therapy,[5] and tissue repairing;[6] there have been very limited reports of a magnetic nanoparticle based controlled-release system.[7,8] These controlled-release systems are comprised of magnetic iron oxide cores surrounded by organic or inorganic constituents, and can be affected by magnetic force. However, many of these systems fail to maintain "zero release" prior to desired delivery mainly because of the nature of the drug encapsulation. To the best of our knowledge, no controlled-release delivery systems based on magnetic nanoparticles that are stimuli-responsive and capable of "zero premature release" have been reported.

Surface-functionalized mesoporous silica materials have been demonstrated to be excellent hosts of molecules of various sizes, shapes, and functionalities.[9-15] Recent reports on the design of capped and gated mesoporous silica derivatives have shown promise in the generation of controlled-release nanodevices.[16-19] Herein, we report the transmission electron microscopy investigation, endocytosis into cancer cells, and the magnetic force propulsion of cancer cells of a controlled-release delivery system that is based on MCM-41-type mesoporous silica nanorods (MSNs) capped with superparamagnetic iron oxide nanoparticles and is stimuli-responsive and chemically inert to guest molecules entrapped in the matrix.

EXPERIMENTAL

HeLa cell line maintenance: Human cervical cancer (HeLa) cell lines were obtained from American Tissue Culture Collection (ATCC) and were maintained using DMEM (Dulbecco's modified Eagle's medium) supplemented with horse serum (10%), L-glutamine (2.00 mM), penicillin (100 U mL^{-1}), streptomycin (100.0 mg mL^{-1}), and gentamicin (1.0 mg mL^{-1}).

Endocytosis of Fe_3O_4 capped MSNs in HeLa cells for magnetic force propulsion: HeLa cells were seeded onto 6-well plates (1 x 10^5 cells per well with 3.00 mL growth media) 24 h prior to the experiment. After 24 h the wells were seeded with Fe_3O_4-capped MSNs in growth media (0.2 mg mL^{-1}) in growth media. After 10 h, the media was removed and the cells were washed with fresh growth media. Following, the cells were trypsinized with 0.25% trypsin. A magnet was used to keep the cells associated with the magnetic nanoparticles stationary while the remaining (nonmagnetic) cells were removed. The cells that took up the Fe_3O_4-capped MSNs were centrifuged and resuspended in a solution of 4′,6-diamidino-2-phenylindole (DAPI, 100.0 μg mL^{-1}) in PBS (100.0 mM, pH 7.4).

Endocytosis of Fe_3O_4-capped MSNs in HeLa cells for fluorescence confocal examination: HeLa cells were seeded onto 6-well plates with acid cleaned 22 mm^2 cover slips on the bottom(1 x 10^5 cells per well with 3.00 mL growth media) 24 h prior to the experiment. After 24 h the wells were seeded with Fe_3O_4-capped MSNs in growth media (0.1 mg mL^{-1}) in growth media. After 13 h, the media was removed and the cells were washed with PBS. Following, the cells were incubated with a solution of PBS (0.1 M, pH 7.4) with formaldehyde (3.7%) and DAPI (100.0 μg mL^{-1}) for 30 min. After incubating the cover slips were laid cell side down on acid cleaned glass slides and adhered with clear fingernail polish.

Instrumental methods, conditions, and parameters for microscopy measurements: For transmission electron microscopy measurements, a small aliquot was ground with methanol in an agate mortar and pestle. A single drop of this suspension was placed on a lacey carbon coated copper TEM grid and dried in air. The TEM examination was completed on a Philips model CM-30 operated at 300 kV at 69,000-340,000 electron optical magnification.

For fluorescence confocal microscopy measurements, HeLa cells were grown on cover slips as reported above. The fluorescence confocal examinations were completed on a Leica TCS NT confocal microscope with UV, argon, and krypton lasers with excitation wavelengths at 340-458 nm, 488 nm, and 568 nm, respectively.

RESULTS AND DISCUSSION

Following synthesis, some characterizing, and in vitro release investigation; the uncapped MSN, capped MSN, and iron (III) oxide nanoparticle caps were measured by TEM and the endocytosis of the Fe_3O_4-capped MSNs into HeLa cells was investigated.

First, TEM investigation confirmed the rod-shape and the average particle size (200 x 80 nm) of the uncapped, acid functional MSN (linker-MSN) (Figure 1a). Transmission electron microscopy measurements also confirmed the irregular, spherical shape and average particle size (10 nm diameter) of the 3-aminopropyltriethylsilane functional superparamagnetic iron (III) oxide nanoparticles (APTES-Fe_3O_4) (Figure 1b). The 10 nm average pore diameter was chosen, so the pores would be capped but the APTES-Fe_3O_4 is too large to enter the pores (average diameter 3.0 nm). Finally, TEM investigations Fe_3O_4-capped MSNs also provided direct evidence of the distribution of Fe_3O_4 nanoparticles on the organically functionalized linker-MSN material. The Fe_3O_4 nanoparticles are clearly visible as dark areas on the outside edge of the mesopores (Figure 1c). In contrast to the feature observed for Fe_3O_4-capped MSNs, the TEM micrograph of the linker MSNs (Figure 1a) prior to capping with Fe_3O_4 nanoparticles showed smooth edges and a good contrast between the mesoporous channels and the silica matrix.

To investigate the endocytosis and biocompatibility of our system, HeLa (human cervical cancer) cells (10^5 cells mL^{-1}) were incubated overnight with Fe_3O_4-capped MSNs (0.2 mg mL^{-1}) to allow the endocytosis of Fe_3O_4-capped MSNs. The cells that took up Fe_3O_4-capped MSNs were magnetically separated from those that did not. The isolated cells were treated with 0.001% of 4′,6-diamidino-2-phenylindole (DAPI) dye in PBS solution (100.0 mm, pH 7.4) and placed in a cuvette. DAPI is known to form blue-fluorescent complexes with natural double-stranded DNA and has been widely used as a fluorescent dye for nucleus staining. These DAPI-stained, fluorescent cells were first accumulated to the right side wall of the cuvette by applying an external magnetic field—a commercially available grade N45 neodymium iron boron magnet. When the magnet was moved to the left side of the cuvette, the blue-fluorescent HeLa cells were clearly seen to move across the cuvette toward the magnet (Figure 3a–c) indicating that the Fe_3O_4-capped MSNs were indeed endocytosed by HeLa cells. To further confirm the endocytosis of Fe_3O_4-capped MSNs, these HeLa cells were examined by confocal fluorescence microscopy. Green fluorescence was clearly observed within the cell bodies of these HeLa cells upon excitation at 494 nm (Figure 3d), which strongly indicates that the mesopore-encapsulated fluorescein molecules were released inside the cells. A series of fluorescence images of different cross-sections of Fe_3O_4-capped MSNs -containing HeLa cells were obtained by changing the focal depth every 1.2 mm vertically (Figure 4a-f).

As previously reported by Biaglow et al., cancer cell lines express significant amounts of dihydrolipoic acid (DHLA).[20] We believe that the efficient intracellular release of fluorescein was triggered by the high intracellular concentration of DHLA. To visualize the locations of the nuclei, the cells were excited at 358 nm (Figure 3e). The appearance of healthy intact nuclei and the visibility of fully grown, healthy cells by transmission (Figure 3f) suggested that the Fe_3O_4-capped MSNs are biocompatible with HeLa cells *in vitro* under these experimental conditions.

In conclusion, we have confirmed the capping of mesoporous silica nanorods by superparamagnetic iron oxide nanoparticles by transmission electron microscopy. The biocompatibility and efficiency of intracellular delivery of Fe_3O_4-capped MSN system with human cervical cancer cells offer promising potential in utilization of this system to investigate various inter- and intracellular chemical/neurochemical communications in vitro. Furthermore, we demonstrated that this stimuli-responsive controlled release delivery system based on mesoporous silica nanorods capped with magnetic nanoparticles had a magnetic motor effect when in the presence of an external magnetic effect.

FIGURE LEGENDS

Figure 1. Schematic of the stimuli-responsive delivery system (Fe_3O_4-capped MSNs) based on mesoporous silica nanorods capped with superparamagnetic iron oxide nanoparticles. The controlled release mechanism of the system is based on reduction of the disulfide linkage between the Fe_3O_4 nanoparticle caps and the linker-MSN hosts by reducing agents such as DHLA.

Figure 2. Transmission electron microscopy micrographs of **a)** linker MSNs, **b)** APTMS-coated Fe_3O_4 nanoparticles, and **c)** Fe_3O_4-capped magnet MSNs.

Figure 3. **a-c)** Single frames of digital photographs of HeLa cells with Fe_3O_4-capped fluorescein-loaded MSNs traveling across the cuvette, propelled by magnet force. **d-f)** Fluorescence confocal micrographs of HeLa cells after 10 h incubation with Fe_3O_4-capped fluorescein loaded MSNs: **d)** cells excited at 494 nm; **e)** cells excited in

the UV region; **f)** a pseudo-brightfield image, where dark aggregations of Fe_3O_4-capped MSNs s can be clearly observed.

Figure 4. Fluorescence confocal micrographs of HeLa cells after 10 h incubation demonstrating endocytosis of Fe_3O_4-capped MSNs s **(a)-(f).** Each frame represents a focal point with 1.2 μm vertical difference.

FIGURES

Figure 1.

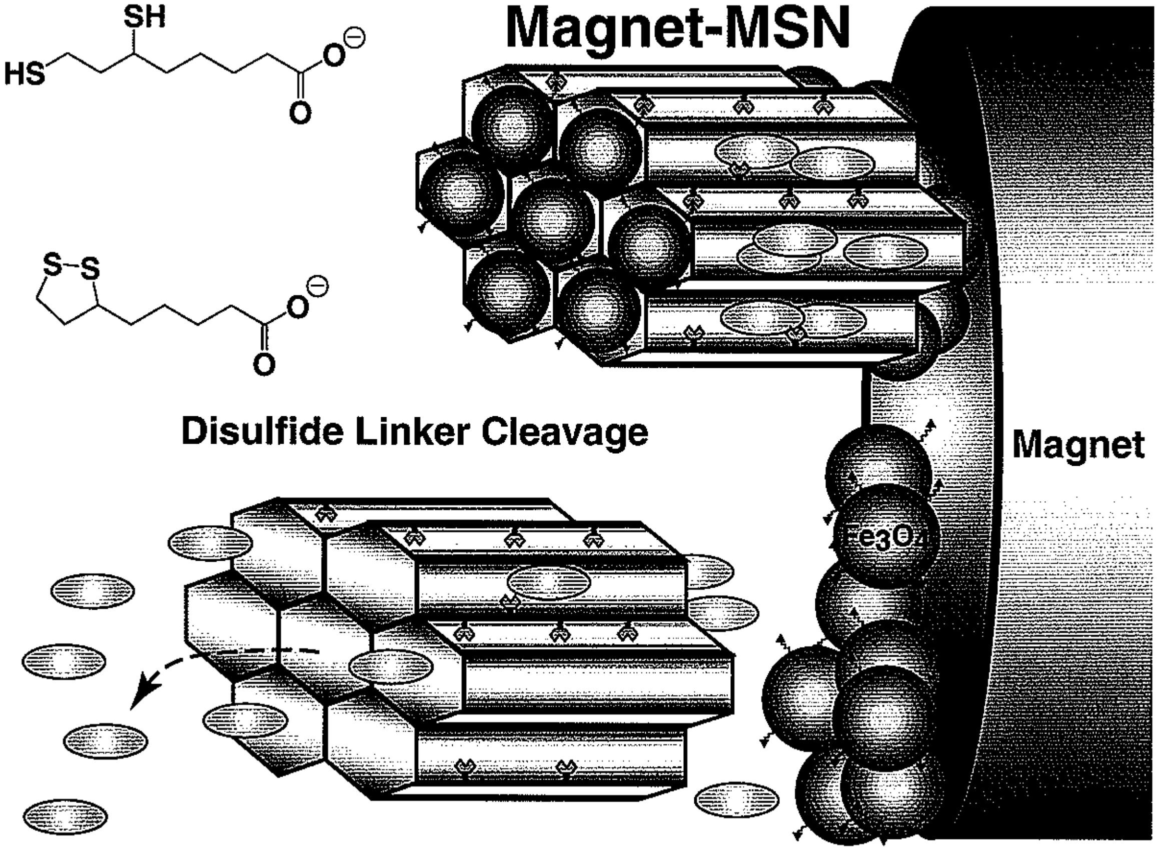

Figure 2.

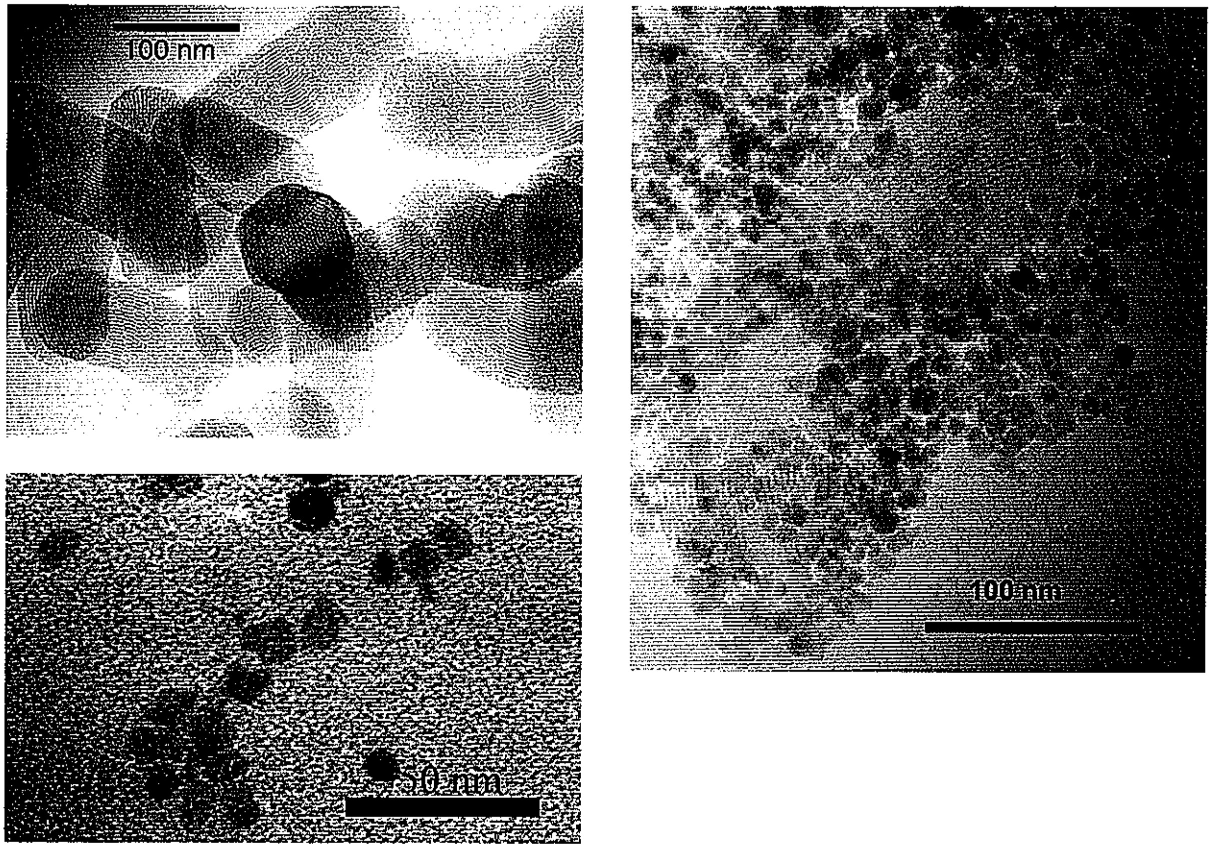

Figure 3.

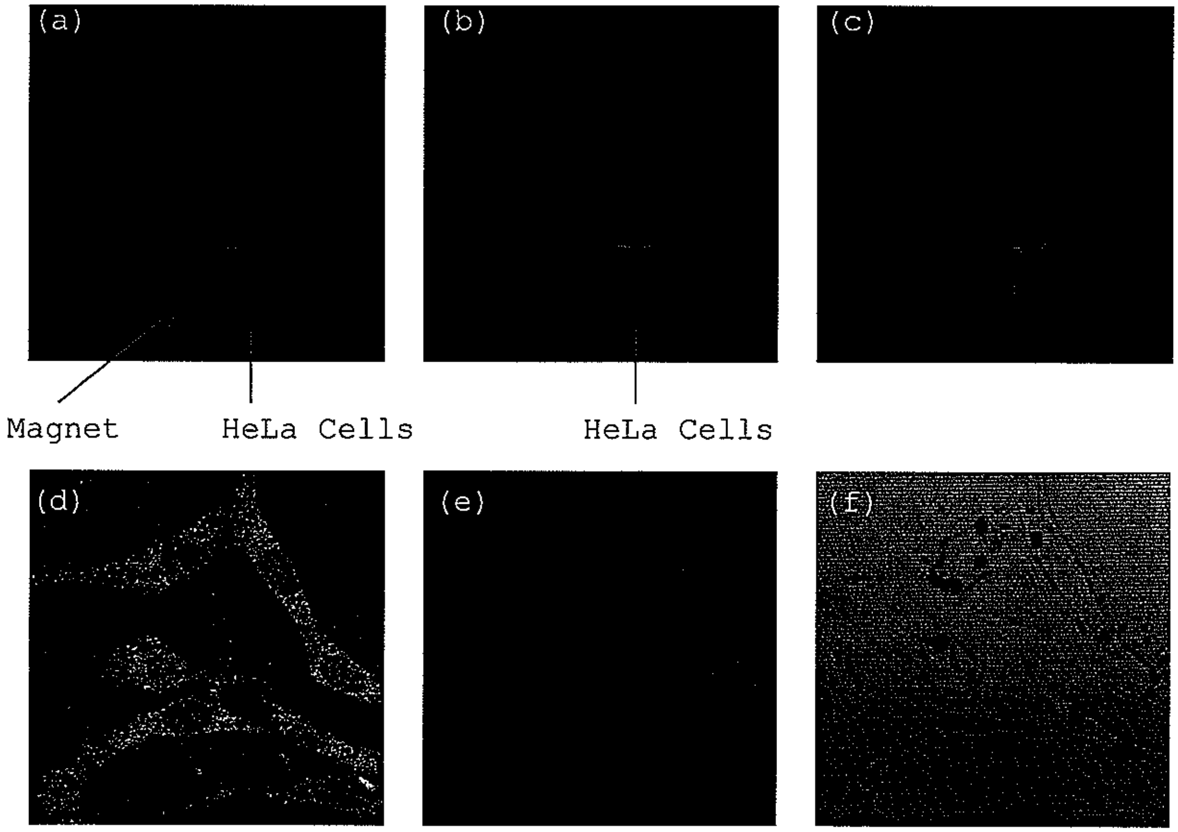

Figure 4.

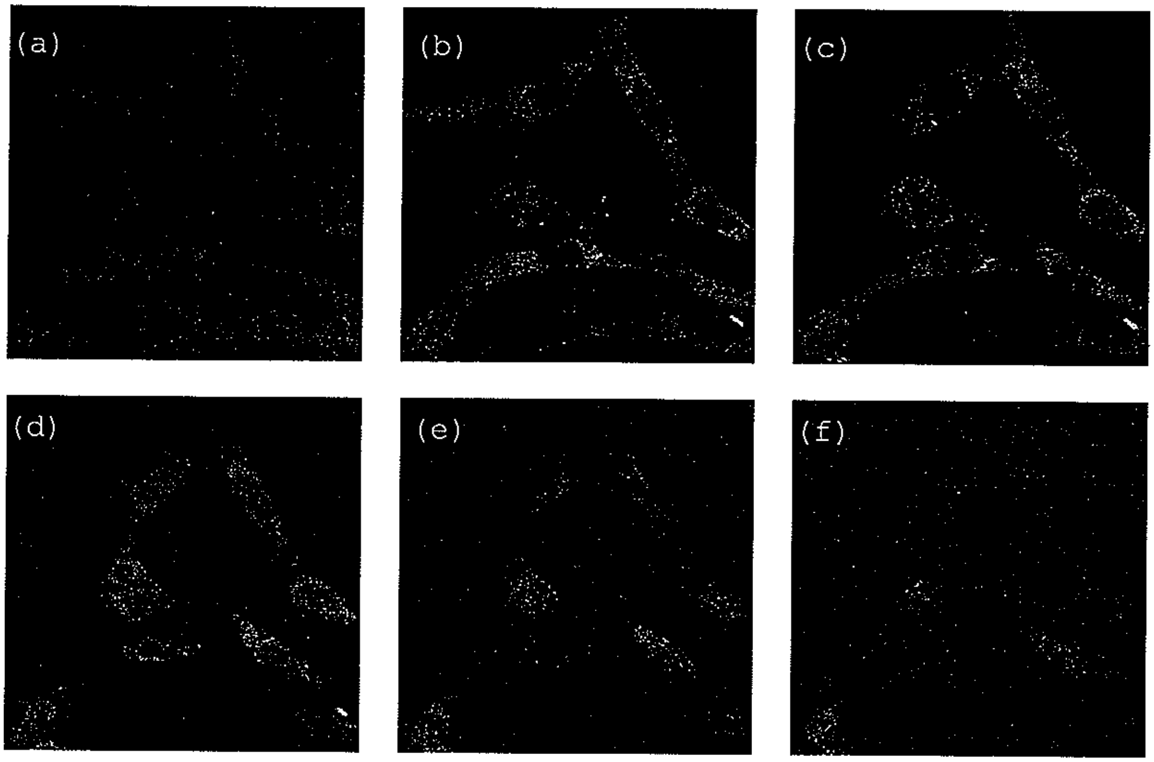

REFERENCES

(1) Gupta, A. K.; Curtis, A. S. G. *Journal of Materials Science: Materials in Medicine* 2004, *15*, 493-496.

(2) Lubbe, A. S.; Bergemann, C.; Brock, J.; McClure, D. G. *Journal of Magnetism and Magnetic Materials* 1999, *194*, 149-155.

(3) Neuberger, T.; Schoepf, B.; Hofmann, H.; Hofmann, M.; Von Rechenberg, B. *Journal of Magnetism and Magnetic Materials* 2005, *293*, 483-496.

(4) Perez, J. M.; Josephson, L.; O'Loughlin, T.; Hogemann, D.; Weissleder, R. *Nature biotechnology* 2002, *20*, 816-20.

(5) Jordan, A.; Scholz, R.; Maier-Hauff, K.; Johannsen, M.; Wust, P.; Nadobny, J.; Schirra, H.; Schmidt, H.; Deger, S.; Loening, S.; Lanksch, W.; Felix, R. *Journal of Magnetism and Magnetic Materials* 2001, *225*, 118-126.

(6) Gupta, A. K.; Gupta, M. *Biomaterials* 2005, *26*, 3995-4021.

(7) Chattopadhyay, P.; Gupta, R. B. *Industrial & Engineering Chemistry Research* 2002, *41*, 6049-6058.

(8) Yoon, T.-J.; Kim, J. S.; Kim, B. G.; Yu, K. N.; Cho, M.-H.; Lee, J.-K. *Angewandte Chemie, International Edition* 2005, *44*, 1068-1071.

(9) Diaz, J. F.; Balkus, K. J., Jr. *Journal of Molecular Catalysis B: Enzymatic* 1996, *2*, 115-126.

(10) Han, Y.-J.; Stucky, G. D.; Butler, A. *Journal of the American Chemical Society* 1999, *121*, 9897-9898.

(11) Munoz, B.; Ramila, A.; Perez-Pariente, J.; Diaz, I.; Vallet-Regi, M. *Chemistry of Materials* 2003, *15*, 500-503.

(12) Ramila, A.; Munoz, B.; Perez-Pariente, J.; Vallet-Regi, M. *Journal of Sol-Gel Science and Technology* 2003, *26*, 1199-1202.

(13) Tourne-Peteilh, C.; Brunel, D.; Begu, S.; Chiche, B.; Fajula, F.; Lerner, D. A.; Devoisselle, J.-M. *New Journal of Chemistry* 2003, *27*, 1415-1418.

(14) Vallet-Regi, M.; Doadrio, J. C.; Doadrio, A. L.; Izquierdo-Barba, I.; Perez-Pariente, J. *Solid State Ionics* 2004, *172*, 435-439.

(15) Vallet-Regi, M.; Ramila, A.; del Real, R. P.; Perez-Pariente, J. *Chemistry of Materials* 2001, *13*, 308-311.

(16) Gruenhagen, J. A.; Lai, C.-Y.; Radu, D. R.; Lin, V. S. Y.; Yeung, E. S. *Applied Spectroscopy* 2005, *59*, 424-431.

(17) Mal, N. K.; Fujiwara, M.; Tanaka, Y. *Nature (London, United Kingdom)* 2003, *421*, 350-353.

(18) Lai, C.-Y.; Trewyn, B. G.; Jeftinija, D. M.; Jeftinija, K.; Xu, S.; Jeftinija, S.; Lin, V. S. Y. *Journal of the American Chemical Society* 2003, *125*, 4451-4459.

(19) Radu, D. R.; Lai, C.-Y.; Jeftinija, K.; Rowe, E. W.; Jeftinija, S.; Lin, V. S. Y. *Journal of the American Chemical Society* 2004, *126*, 13216-13217.

(20) Biaglow, J. E.; Donahue, J.; Tuttle, S.; Held, K.; Chrestensen, C.; Mieyal, J. *Analytical biochemistry* 2000, *281*, 77-86.

CHAPTER 5. TRANSMISSION ELECTRON MICROSCOPY INVESTIGATION INTO MESOPOROUS MATERIAL AND RELATED STRUCTURES

Brian G. Trewyn and Victor S.-Y. Lin

ABSTRACT

An important characterization technique for the synthesis and application of mesoporous material is transmission electron microscopy. Here we present a survey of some of the mesoporous materials produced in our lab. Included are brief explanations of each project, along with TEM micrographs of the materials.

INTRODUCTION

Since the invention of the first simple light microscope in 1673 by Antoni van Leeuwenhoek, the field of microscopy has developed incredibly to a point where light is no longer the sole image forming source. Electrons are now used to visualize the details of the microstructural characterization of materials. Electron microscopy is simply defined as the science and technology of using a beam of electrons to produce magnified images of specimens.[1]

The invention of the modern day transmission electron microscope (TEM) could not have been made without the work of numerous scientists, many of whom went on to become Nobel laureates. In 1897, J.J. Thomson discovered the electron, work he received the Nobel Prize in Physics for in 1906. Thomson demonstrated that an electron is a particle of very small mass, with a negative charge, and can be deflected by electric and magnetic fields. Prince de Broglie, winner of the Nobel Prize in Physics in 1929, defined the wave nature and wavelength of electrons.

Two individuals are credited with the discovery of the transmission electron microscope in the early 1930s, Max Knoll and Ernst Ruska of the High Voltage Laboratory at the Technological University in Berlin. As part of his student thesis, Ruska built the first operational TEM in 1933.[2,3] Ruska is also credited with building the first electromagnetic lens suitable for use in an electron microscope to direct the electron beam.[4] Ruska was awarded the Nobel Prize in Physics in 1986, along with Gerd Binning and Heinrich Rohrer for their work on the design of the scanning tunneling microscope. In presenting the award, the Nobel Prize Committee noted the significance of electron microscopes in all areas of science, calling them "one of the most important inventions of the 20th century.[1]"

The main advantage of using electrons as the image-forming source instead of light is resolution (the ability to distinguish fine detail). The resolving power of a modern light microscope is 200 nm, whereas a TEM can resolve detail to approximately 0.2 nm. Electrons are produced for the imaging beam by an electron gun.

The electron gun is composed of an anode, a Wehnelt assembly, and a wire filament (electron source). The three major types of electron gun are tungsten-hairpin filament, lanthanum-hexaboride [LaB_6] hairpin filament, and the field emission gun. The first two employ thermionic emission, in which the electrons are produced by heating the filament by applying a small voltage differential across the terminals of the filament. The LaB_6 gun has several advantages over the tungsten gun. The advantages include a ten-fold increase in beam current and a more narrow point at which the electrons are emitted. The increased beam current is directly related to the beam brightness, while the narrow emission point decreases the energy spread of the emitted electron by one-half that of the tungsten-filament gun. Both advantages lead to greater resolution with the LaB_6 gun.

The third type of gun, field-emission, gives the best resolution. In high vacuum, electrons are physically drawn off a very finely curved tungsten tip with an applied voltage. The resolution of a field emission gun is improved over a thermionic gun, because of the much greater brightness, and an electron beam of smaller diameter. Finally, a longer lifetime can be expected from a field emission gun over thermionic guns.

After the beam of electrons is formed and passed through the anode, it is controlled by electromagnetic lenses. The beam of electrons passes through the opening in the center and is focused and deflected by magnetic lines of force. These lenses, called pole pieces, concentrate all of the magnetic lines of force in the gap, creating a very powerful lens. All electromagnetic lenses are controlled and focused by varying the electrical current through the lens. In addition to the electromagnetic lens, the electron beam is controlled by apertures. The primary use of these apertures is to limit the diameter of the beam and to eliminate stray or widely scattered electrons.

Two lens—aperture separate assemblies are used to control different aspects of specimen imaging. The condenser-lens system controls illumination. The objective lens is the most important and complex lens in a TEM because it is the first magnifying lens. The apertures equipped with the objective lens also control the contrast; the smaller the objective aperture, the greater the contrast. As with many aspects of the TEM, a compromise must be reached between the brightness (condenser assembly) and contrast (objective assembly).

Research in the field of material synthesis, characterization, and application requires transmission electron microscopy measurements to determine size, morphology and porous structure. Reviewers and critics of this area of research require TEM evidence to verify our results and conclusions. The following is a short survey on the work we did on various projects using the TEM.

EXPERIMENTAL

All TEMs reported, discussed, and presented in this chapter were measured on a Philips model CM-30 transmission electron microscope operated at an accelerating voltage of 300 kV. Sample preparation varied from specimen to specimen.

The solid samples were suspended in water, methanol, or acetone, depending on the hydrophobic or hydrophilic nature of the sample. Following a short sonication the suspensions were placed on an ultrathin carbon film supported by a lacey carbon film on a 400 mesh copper grid via syringe. When the suspendant was water, the grid was placed on a hot plate to expedite the evaporation of the water; the organic suspendants were left at room temperature to evaporate. Some of the specimens presented here necessitated ultramicrotoming for further investigation of the pore structure.

The preparation of ultramicrotomed samples included embedding the samples in EPON epoxy resin using EmBed 812. The specimens were suspended in the epoxy, centrifuged, and cured for 24 h at 60 °C followed by 24 h at 70 °C. Following the heat treatment, the embedded block was microtomed using a Leica Reichert Ultracut T ultramicrotome with a Diatome diamond knife to a thickness of 60 - 100 nm. Once microtomed, the section was floated on to the same lacey carbon - 400 mesh copper grid. The microtomed samples were also measured on the Philips model CM-30 TEM operating at 300 kV. Some ultramicrotomed samples required reduction of the spot size to avoid destruction of the section under the high voltage beam bombardment.

The measurements were recorded on Kodak Electron Image Film SO-163. The negatives were then developed by submersion into first Kodak D-19 Professional Developer, followed by Kodak Professional Fixer, for equal amounts of time. All Kodak materials are from the Eastman Kodak Company.

The developed micrographs were then scanned into a computer to get digital images. The Adobe Photoshop software was then used to crop the micrographs to desired size and to accurately add scale bars.

RESULTS AND DISCUSSION

Transmission electron microscopy investigations began with the synthesis and application of an MCM-41 type mesoporous silica nanosphere-based (MSN) controlled-release delivery system. The MSN was capped with chemically removable CdS nanocrystals to encapsulate several pharmaceutical drug molecules and neurotransmitters inside the mesoporous framework.[5] Transmission electron micrographs of the uncapped and capped MSN are presented in figure 1a-d. By using disulfide bond-reducing molecules as release triggers, the stimuli-responsive release profiles of vancomycin- and adenosine triphosphate (ATP)-loaded MSN were studied (Figure 1e). The biocompatibility and delivery efficiency of the MSN system with astrocytes *in vitro* were also demonstrated.

The second project presented here is unique in that the material synthesized templated by anionic sodium dodecyl sulfate surfactant. Using a novel method, a mesoporous silica-supported uranyl material ($U_{aq}O_2^{2+}$-silica) were prepared by a co-condensation method under acidic conditions.[6] An application of this material involved an excitation of aqueous suspensions of $U_{aq}O_2^{2+}$-silica in the visible or near-UV region and photocatalyzing the oxidation of alcohols with O_2 (Figure 2a). The material was not MCM-

41 type; i.e. it had a disordered pore arrangement. The TEM micrographs (Figure 2b and 2c) showed a wormhole-like porous structure, which confirmed the observation in the surface sorption BET studies.

Another project, reported in 2003, introduced the development of a synthetic method that can control both the multifunctionalization and morphology of mesoporous organic-inorganic hybrid materials and was reported in 2003.[7] The morphology can be controlled by introducing different molar ratios of organoalkoxysilane precursors to a base-catalyzed co-condensation of silicate. One example of this morphology control was measured by TEM (Figure 3). By incorporating 12.8 mol% cyanopropyltriethoxy-silane (CPTES) in the material synthesis, a rod-shaped morphology was observed with an average size of 1 x 0.2 μm, in contrast to pure MCM-41, which exhibits irregular spherical shapes. The multifunctionalization of the materials with two organoalkoxysilanes, 3-[2-(2-aminoethylamino)ethylamino]-propyltrimethoxysilane (AEPTMS) and CPTES, demonstrated the incorporation of differing ratios of the two organoalkoxysilanes resulted in spherical particles of differing sizes and degrees of polydispersity. Since all the AEPTMS functionalized materials showed spherical morphology, and no rod-shaped particles were formed from the bifunctional material, it was concluded that the presence of AEPTMS precursor in the co-condensation reaction played a crucial role in governing the particle shape.

Calcia-silica materials were prepared via a co-condensation method under basic conditions. The calcium is incorporated into the silica framework, as opposed to discrete calcium oxide crystalline sites. The materials can be utilized as catalysts for the esterification of biomass feedstocks, such as soybean oil and poultry fat, by reaction of the feedstock with catalyst in methanol at elevated temperatures. Biodiesel methyl esters result, and the catalyst may be reused in successive esterification reactions. Three materials were synthesized, each with a different amount of calcium oxide incorporated. The higher calcium oxide content materials catalyzed the esterification of biomass to biodiesel methyl esters with faster conversion rates.

An inorganic-organometallic hybrid material in which a palladium organophosphine complex was integrated into the pore walls of highly ordered microstructured silica (Pd-PMO) as synthesized by co-condensation. This material catalyzed the Suzuki coupling reaction of ethyl 4-bromobenzoate with phenylboronic acid, and exhibits high recyclability. This material was challenging in that the average pore diameter could not be accurately determined by conventional nitrogen surface sorption analysis, since the average pore diameter was below 20 Å. The TEM micrograph was used to determine a pore size of 19 Å by digitally measuring the distance between two parallel lanes of the silica framework (Figure 5a). Another interesting aspect of this material is its biphasic. The material possesses regular, hexagonal parallel pore structure in selected areas (Figure 5a) and, other areas of wormhole pore structure (Figure 5b). Both types of pore structure seem to form within close proximity (Figure 5c). The reason for the biphasic nature of the material is unclear, but a possible contributing factor is that the synthesis includes both aqueous and organic solvents. The organoalkoxysilane is suspended in acetonitrile, while the silane monomer is hydrolyzed in an acidic aqueous phase.

Transmission electron microscopy is an important characterization technique to investigate the synthesis and application of mesoporous material. Here we presented the TEM images and gave short reviews of mesoporous materials produced and applied in our lab for use in biological and catalytic systems.

FIGURE LEGENDS

Figure 1. Transmission electron micrographs of microtomed amine functional MSN **(a and c)** and microtomed CdS nanoparticle capped ATP loaded MSN (b and d). The first two micrographs (a and b) are orientated so the pores are orthogonal to the electron beam, while the second two micrographs **(c and d)** are orientated parallel to the electron beam. The mesoporous channel structure of the nanoparticles is visualized with the parallel stripes **(a and b)** and the hexagonally packed light dots **(c and d)** shown in the micrographs. The labile linker is a reducible disulfide linkage. The blue arrows indicate the aggregation of CdS nanoparticles on the exterior surface of the MSN material. The green arrow indicates an area, which the MSN is capped by the CdS, displayed by light dots packed in a disordered symmetry. An uncapped region is indicated by the red arrow, where the hexagonal arranged pores is readily visible. Schematic representation of the CdS nanoparticle-capped MSN based drug/neurotransmitter delivery system **(e)**.

Figure 2. Transmission electron micrographs of microtomed mesoporous silica-supported uranyl material synthesized by the co-condensation method **(a and b)**. A schematic representation of the chemical nature inside the pores and the photochemical reaction that is catalyzed by the $U_{aq}O_2^{2+}$-silica **(c)**.

Figure 3. Transmission electron micrograph of 3-cyanopropyl functionalized MSN synthesized by the co-condensation method.

Figure 4. Transmission electron micrographs of calcia-silica material synthesized by the co-condensation method under basic conditions.

Figure 5. Transmission electron micrographs of the Pd-PMO material synthesized by the co-condensation method under acidic conditions **(a-c)**. The red arrows indicate the hexagonally ordered parallel pores, and the blue arrows indicate the worm-hole, disordered pores.

FIGURES

Figure 1a-d.

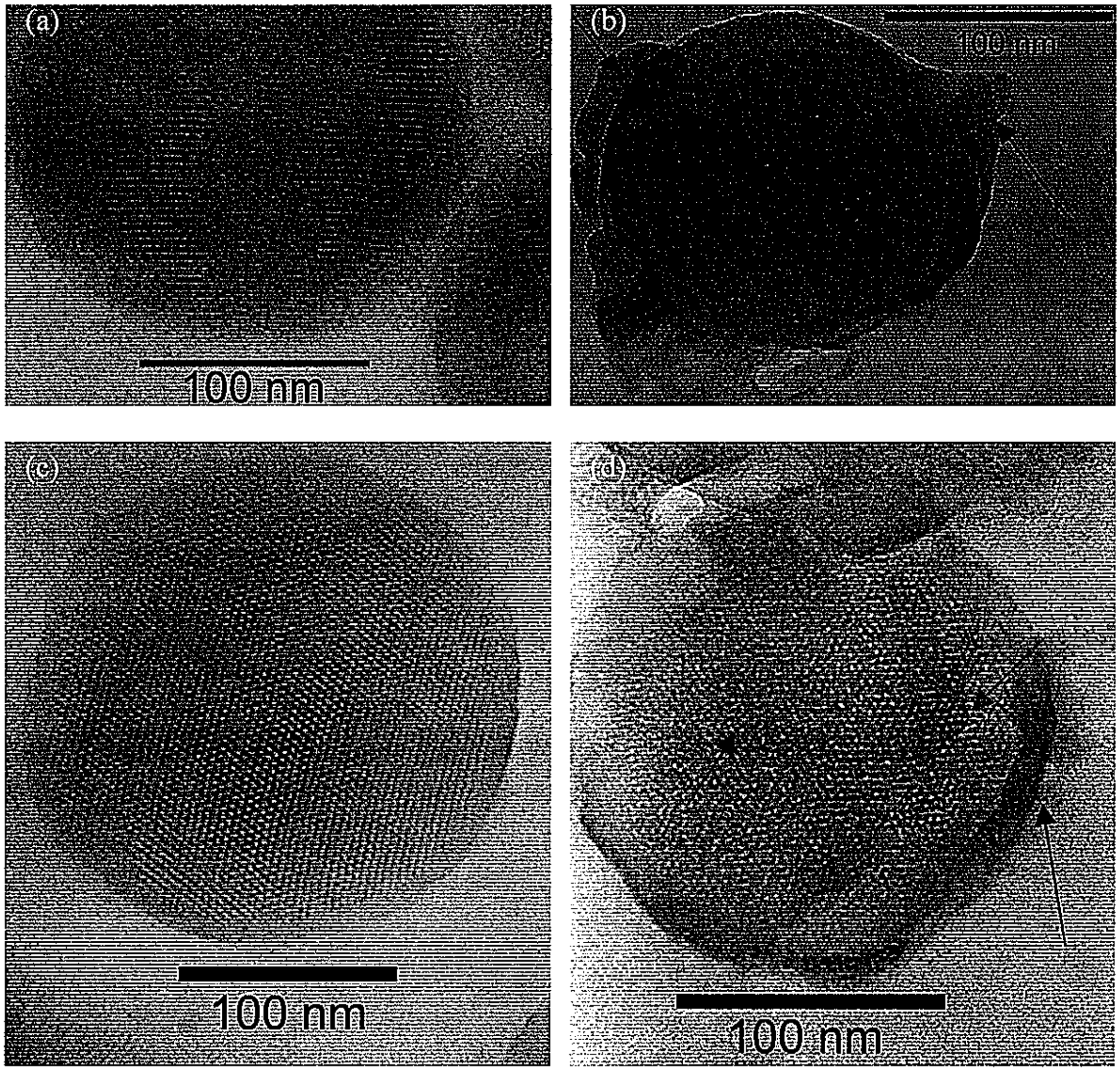

Figure 1e.

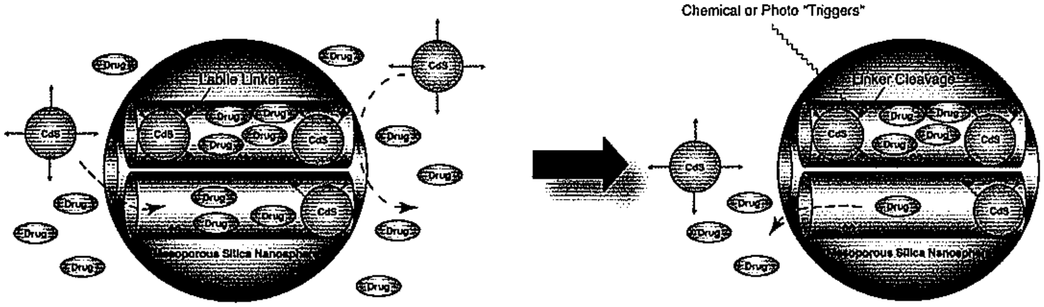

Capping

Uncapping

Figure 2.

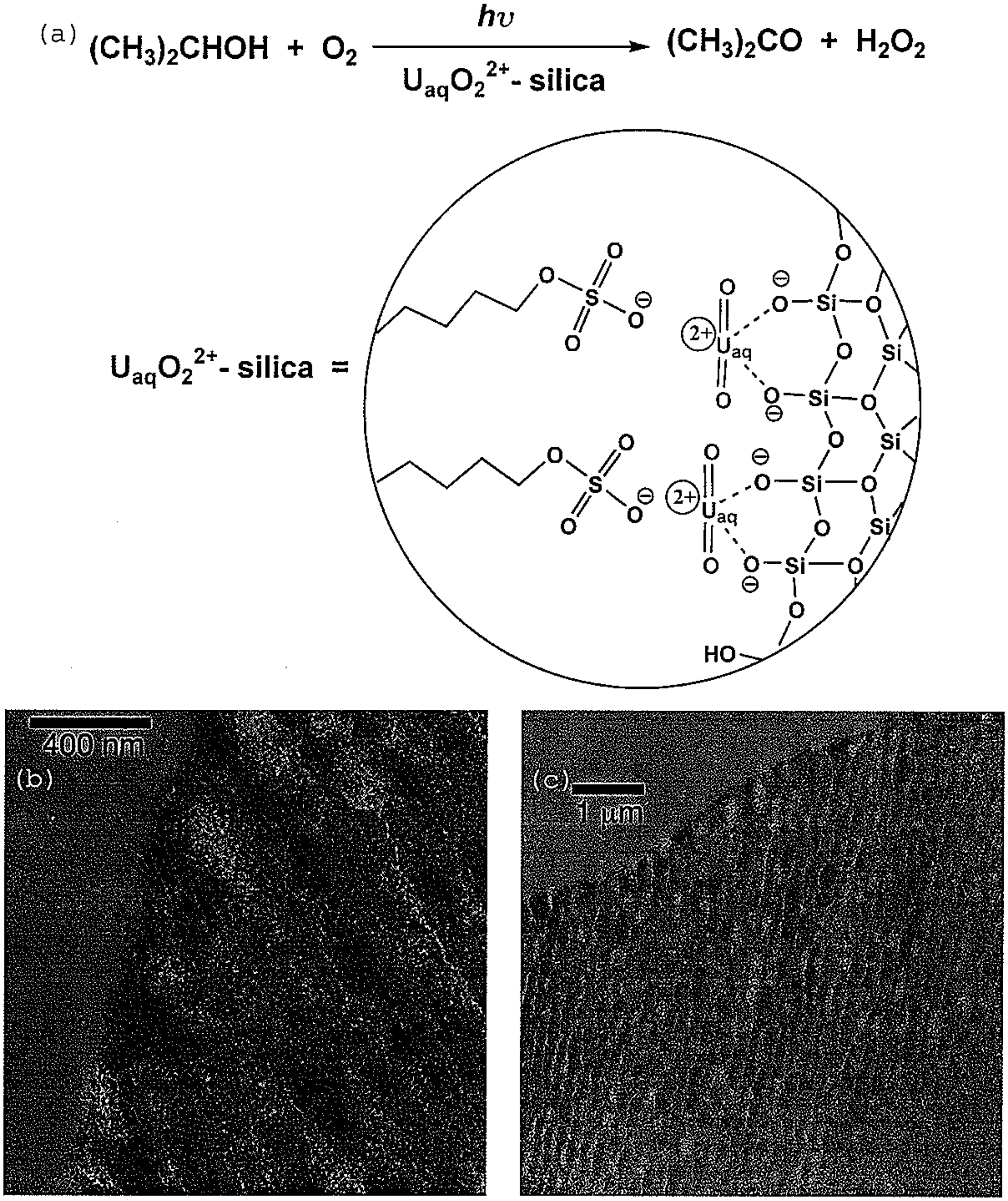
(a)
(CH3)2CHOH + O2
hυ
UaqO2 2+- silica
(CH3)2CO + H2O2
UaqO2 2+- silica =
2+
Uaq
Si
HO
(b)
400 nm
(c)
1 μm

Figure 3.

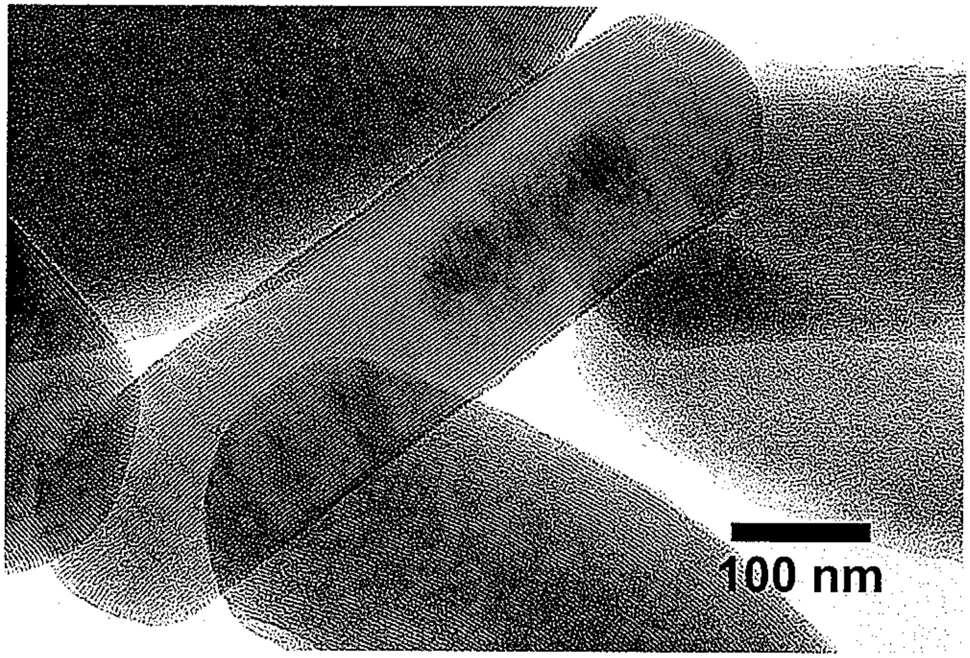

Figure 4.

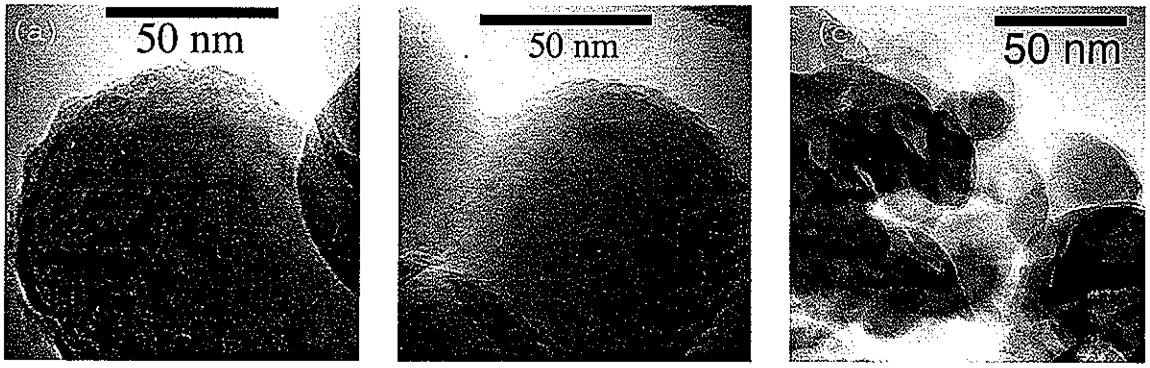

Figure 5.

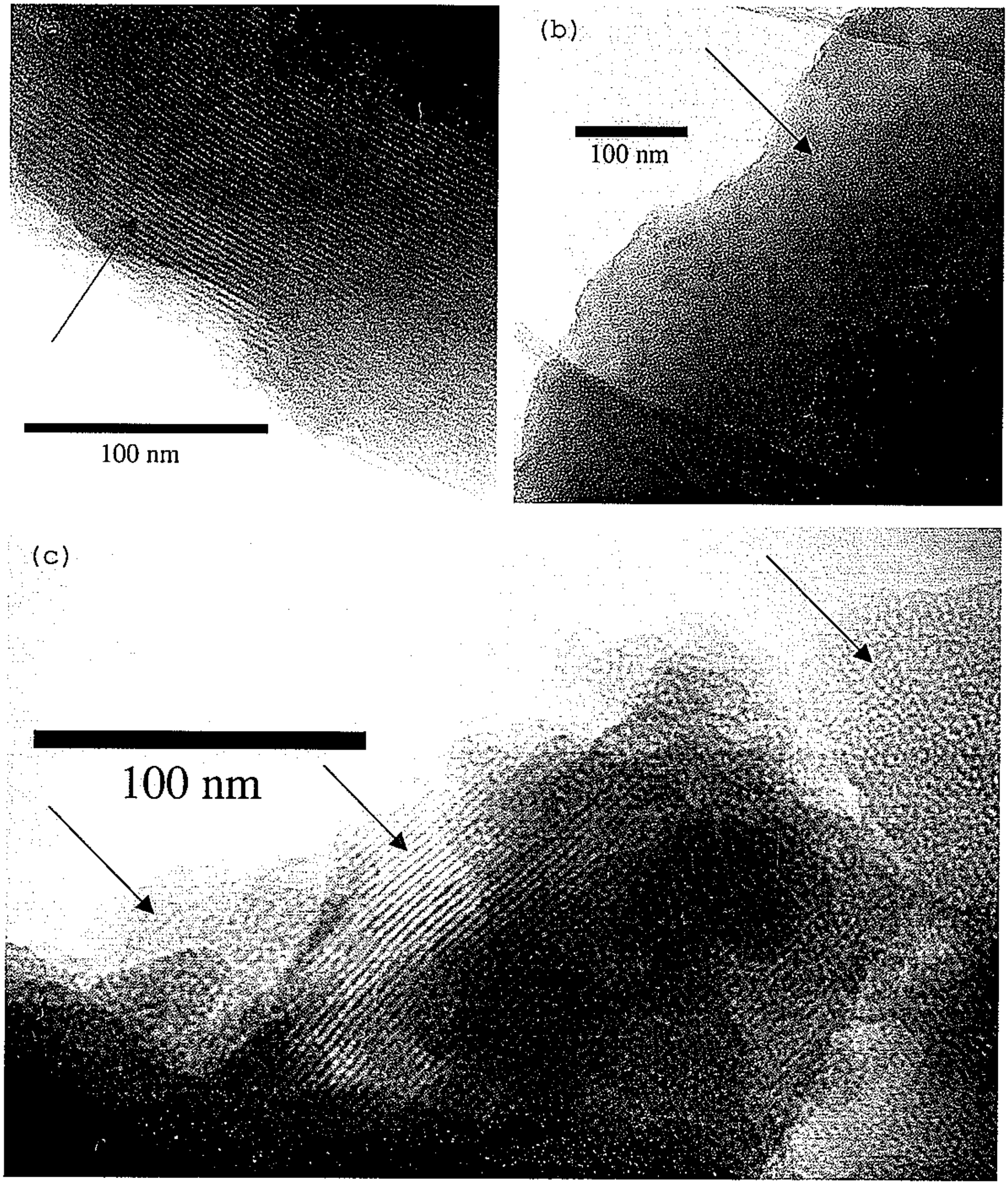

REFERENCES

(1) Flegler, S. L.; Heckman, J. W., Jr; Klomparens, K. L. *Scanning and Transmission Electron Microscopy: An Introduction*; Oxford University Press: New York, 1993.

(2) Ruska, E. *Zeitschrift fuer Physik* **1933**, *83*, 492-7.

(3) Knoll, M.; Ruska, E. *Zeitschrift fuer Physik* **1932**, *78*, 318-39.

(4) Ruska, E. *Zeitschrift fuer Physik* **1934**, *89*, 90-128.

(5) Lai, C.-Y.; Trewyn, B. G.; Jeftinija, D. M.; Jeftinija, K.; Xu, S.; Jeftinija, S.; Lin, V. S. Y. *Journal of the American Chemical Society* **2003**, *125*, 4451-4459.

(6) Nieweg, J. A.; Lemma, K.; Trewyn, B. G.; Lin, V. S. Y.; Bakac, A. *Inorganic Chemistry* **2005**, *44*, 5641-5648.

(7) Huh, S.; Wiench, J. W.; Trewyn, B. G.; Song, S.; Pruski, M.; Lin, V. S. Y. *Chemical Communications (Cambridge, United Kingdom)* **2003**, 2364-2365.

CHAPTER 6. GENERAL CONCLUSIONS

Research into the field of mesoporous materials vast vast and ever expanding field due to the growing number of possible applications available. Mesoporous material exhibits numerous characteristics, including high surface area, varying pore size, large specific pore volume, chemical inertness, and biocompatibility. These materials may be functionalized, loaded with host molecules, capped, and used as controlled release vehicles; functionalized mesoporous materials have also been shown to effectively catalyze various reactions. Examples of both these biological and catalytic applications are reported and discussed within.

First, a series of ionic liquid (IL) containing mesoporous silica nanoparticle materials with various particle morphologies was synthesized. By changing the IL template, the pore morphology was tuned from the MCM-41 type of hexagonal mesopores, to rotational moiré type of helical channels, and finally to wormhole-like porous structures. These materials were used as controlled release delivery nanodevices to release antibacterial ionic liquids against *E. coli.*

The effect of a specific organosiloxane functional group covalently attached to the exterior of fluorescein doped mesoporous silica nanoparticles on the degree and kinetics of endocytosis into cancer and plant cells was investigated. The kinetics of endocystosis of TEG coated FITC-MSN is significantly quicker, than FITC-MSN as determined by flow cytometry experiments. The fluorescence confocal microscopy investigation showed the endocytosis of TEG coated-FITC MSN into both HeLa cells and Tobacco protoplasts.

Once the synthesis of a controlled-release delivery system based on MCM-41-type mesoporous silica nanorods capped with superparamagnetic iron oxide nanoparticles was completed, the material was characterized, and the dosage and kinetics of the antioxidant dependent release was determined; the TEM measurements were recorded and the biological interaction of the material with cancer cells was determined. The electron microscopy investigation proved that the pore openings of the MSN were indeed blocked by the Fe_3O_4 nanoparticles. The biological interaction investigation demonstrated Fe_3O_4-capped MSN endocytosis into

HeLa cells. Not only does the material enter the cells through endocytosis; but also it seems the fluorescein was released from the pores, likely caused by cell-producing disulfide bond reducing molecules. Upon endocytosis, the Fe_3O_4-capped MSNs were able to propel the cells across a cuvette upon induction of a magnetic force.

Finally, an important aspect of nanostructured material characterization is transmission electron microscopy (TEM) and the importance of a complete TEM investigation was shown for the various materials produced. It was demonstrated that incorporating different functional groups (organic and inorganic) during the synthesis (co-condensation) changes the particle and pore morphologies.

One of the most promising directions of mesoporous material is its fusion with biology and biotechnology. Future possible applications of this material include the intracellular controlled release of drugs and cellular markers from the pores. If the pores can be loaded with highly active anti-cancer drugs and released selectively in cancer cells, then some of the detrimental side effects of the current "shotgun" approach to cancer therapy can be avoided. The pores may similarly be loaded with fluorescent cell markers and released after the mesoporous nanoparticles enter the cell. Currently, cells are labeled by endocytosis of ester protected fluorescent tags, and the rate of intracellular diffusion cannot be controlled. If, at a later date, the rate of uncapping of the MSN can be controlled then it may be possible to record some cellular functions that are currently not observable.

In addition to the applications discussed in this dissertation, various other potential applications in microelectronics, sensors, and molecular wires are currently being exploited. These potential research opportunities will continue to expand with the development of new surface and framework modification techniques, pore structure, and composition.